Periodico di Mineralogia
ISSN: 0369-8963

Volume 94, No. 2, 2025

Mineral-chemistry and geochemistry of pyroxenite xenoliths in trachytic and leucitite lavas of the Islamic Peninsula (Northwest of Iran - East of Lake Urmia)

Mousa Akbarzadeh Laleh[1], Nasir Amel[2], Mohsen Moayyed[2]

1- PhD student in Geology-Petrology, University of Tabriz

2 - Faculty member, Faculty of Natural Sciences, University of Tabriz

Abstract

The Islamic Peninsula (Saray Volcano) is located east of Lake Urmia and west of Sahand Volcano. It is composed of alternating lava flows and pyroclastic deposits, subsequently intruded by dikes and dome structures. The dominant trachytic and leucitite lava flows contain xenoliths of varying sizes and morphologies. The primary minerals in the trachytic host rock include sanidine, biotite, and opaque minerals. In contrast, the leucitite host rocks are mainly composed of leucite and clinopyroxene, set within a fine-grained groundmass of leucite, clinopyroxene, olivine, and opaque minerals. The boundary between the host rock and xenoliths is sharp, lacking any reaction rims. The xenoliths primarily consist of clinopyroxene, biotite, and apatite. Some clinopyroxene and biotite crystals within the leucitite xenoliths display elongated and oriented textures. The clinopyroxene compositions in both the xenoliths and the trachytic and leucitite host rocks range from diopside to fassaite. Micas in the trachytic host rock and associated xenoliths are biotite and phlogopite, whereas those in the leucitite host rock and its xenoliths are exclusively phlogopite. The micas within the leucitite host rock and xenoliths are primary biotites, whereas those in the trachytic host rock exhibit both primary and recrystallized biotite phases. The estimated crystallization temperatures for clinopyroxenes in the trachytic and leucitite xenoliths and host rocks range between 1200–1300°C. Specifically, clinopyroxenes in the trachytic host rock formed at temperatures of 1027–1111°C, while those in the leucitite host rock crystallized between 996–1143°C and 1044–1140°C. The calculated pressure for clinopyroxenes in both rock types is approximately 6–10 kbar, corresponding to an estimated depth of 20–35 km. The negative Ti, Nb, and Ta anomalies in the leucitite host rock suggest varying degrees of crustal contamination and a possible association with subduction-related active continental margin settings. The close similarity in the Mg-number of clinopyroxene and biotite in both xenoliths and host rocks indicates a common parental magma. However, subsequent heteromorphic differentiation under distinct physico-chemical conditions resulted in the formation of compositionally similar but mineralogically different rock types. The mantle source of the Saray volcanic activity is identified as a phlogopite-bearing garnet lherzolite.Structurally, two major fault zones, the ENE-WSW trending Saray-Aq Gonbad fault and the SSE-NNW trending Teymurlu-Gamichi fault, intersect in the central part of the peninsula, creating a fractured and weakened zone that facilitated magma ascent. The ascending magma underwent crystallization in magma chambers, forming cumulate phases that were later transported to the surface by magmatic eruptions.

Key words: Islamic Peninsula - Saray Volcano - Xenolith - Pyroxenite

https://doi.org/10.5281/zenodo.15010171

Introduction

The Islamic Peninsula (Saray Volcano) is located in the western part of the Alborz-Azerbaijan region and the northern section of the Urmia-Dokhtar magmatic belt, within the Iranian-Turkish high plateau, as classified by Iran's structural zones (Nabawi, 1976). The volcano lies east of Lake Urmia and west of the Sahand Volcano. It consists of alternating lava and pyroclastic deposits. The Saray Volcano is a stratovolcano cone, later intruded by domes (Moayyed et al., 2013). The primary outcrops in this stratovolcano include a sequence of tephrite, leucite-tephrite, basanite, leucite-basanite, trachyte, and associated pyroclastic rocks (Moayyed et al., 2013). Dykes with similar lithology, as well as lamprophyre dykes, are also observed in the region, particularly in the central parts of the stratovolcano. The absolute age of certain minerals, determined using the K-Ar method, revealed a crystallization age of 6.1 ± 0.5 million years for biotites in trachytic rocks (Moradian Shahrbabaky, 2007). For tephrite (whole rock), the age was 7.8 ± 0.29 million years (Moein-Vaziri, 1985), and for tephrite-phonolite (whole rock), it was 23.5 ± 1.2 million years (Bina et al., 1986). The dating, geochemical, and isotopic data of Saray rocks suggest that late Miocene magmas formed from low-degree melting of a subduction-enriched lithospheric mantle source in a post-collisional tectonic setting (Shafaii Moghadam et al., 2014). Xenoliths are found in lavas, dykes, and pyroclastics across the Islamic Peninsula. Studying these xenoliths is crucial as they provide valuable evidence about magma origins and magmatic processes in the reservoir, such as mineral segregation, fractional crystallization, and subsequent geochemical evolution. This area contains various xenoliths, including clinopyroxenite xenoliths. Similar xenoliths are observed in regions such as the Kapwal craton (Gurney et al., 1975), Jericho craton, and Slave craton (Kopylova et al., 1999). Numerous researchers have examined the volcanic rocks and xenoliths of the Islamic Peninsula (Sepidbar et al., 2023; Ghaderi et al., 2022; Basharti et al., 1999; Moine-Vaziri et al., 1991; Moayyed et al., 2008; Ghaderi et al., 2020). Geochemical analyses reveal that rocks in this area are MgO-rich basic rocks (MgO = 8.0–13.9 wt%; SiO_2 = 46.1–50.9 wt%) such as mafic lamprophyres and pyroxenitic xenoliths, as well as MgO-poor rocks (MgO = 1.5–6.4 wt%; SiO_2 = 48.2–61.2 wt%) including trachytes, felsic lamprophyres, tephrite-phonolites, and analcime-bearing phenotephrites (Sepidbar et al., 2023). Both high- and low-MgO samples exhibit strong radiogenic ratios: $(^{87}Sr/^{86}Sr)_i$ = 0.7078–0.7086, $(^{143}Nd/^{144}Nd)_i$ = 0.51244–0.51235 (below the chondritic uniform reservoir, CHUR), and Hf ε values ranging from -3.1 to -11.1%. These characteristics suggest the involvement of a lower continental crust component in their origin. The major oxide and trace element contents in MgO- and CaO-rich rocks indicate derivation from a subcontinental lithospheric mantle variably metasomatized by fluids and melts released from a subducted slab within a mantle wedge. The primary melts evolved through the fractionation of mafic minerals and possible assimilation of lower crustal material, leading to the differentiation of higher SiO_2 and lower CaO-MgO groups. Partial melting of enriched mantle sources could have been triggered by the rollback of the Neo-Tethys slab during the Arab-Iranian collision (Sepidbar et al., 2023). Investigating pyroxenite xenoliths in the trachytic and leucitite lavas of the Islamic Peninsula provides critical insights into their origin. This research aims to analyze the lithology and mineral chemistry of the clinopyroxene-rich xenoliths from the Saray Volcano and calculate the temperature and pressure conditions during the formation of these rocks.

Geology of the region

Cenozoic volcanic rocks are concentrated in the eastern region of Azerbaijan, forming a volcanic plateau surrounded by Neogene depressions (Didon and Gemain, 1976). Structurally, this region is part of the Alpine volcanic belt and has undergone multiple magmatic events. Studies of the Tertiary magmatism in Western Alborz-Azerbaijan reveal that the Eocene volcanic rocks of this area are calc-alkaline with high potassium and shoshonitic compositions, indicative of formation in a post-collisional tectonic environment (Moayyed, 2012). Unlike the Paleogene period, when volcanic activity primarily occurred through fissure eruptions and feeding dykes, Neogene volcanism in Iran is characterized by central-type eruptions and the formation of stratovolcanoes. However, in some instances, extensional fractures facilitated magma escape (Emami, 2009). One such example is the Islamic Volcanic Island, which features two prominent faults: the Saray-Aghgonbad fault trending ENE-WSW and the Timorlo-Gamichi fault trending SSE-NNW. The intersection of these faults is near the central part of the peninsula (Hajalilou et al., 2009). From a geo-structural perspective, the magmatism of this region belongs to the Tertiary-Quaternary magmatic zone. The highlands of the Islamic Peninsula are morphotectonically distinct from the Sahand volcanic highlands. Gravity field variations in this region range between -110 and -100 milligal, and the crustal thickness is approximately 42 to 43 km. The Islamic Island primarily consists of alternating layers of lavas and pyroclastics (Figure 1-A). The lithological composition of the lavas predominantly includes saturated and undersaturated rocks, which are intersected by dykes and later intrusive rocks (Figure 1-B, C and D). Many of these lavas, pyroclastics, dykes, and intrusions contain xenoliths, whose sizes vary considerably, occasionally reaching up to 20 cm in trachytic rocks. This research focuses on the xenoliths embedded in the trachytic and leucitite host rocks of the region. These xenoliths exhibit diverse shapes, with most being rounded, while some are polygonal. The majority are black with a somewhat shiny surface (Figure 2). The southern half of the Islamic Island contains a higher abundance of xenoliths compared to the northern half. This distribution correlates with the widespread occurrence of trachytic lavas and pyroclastics in the southern part of the island (Figure 3).

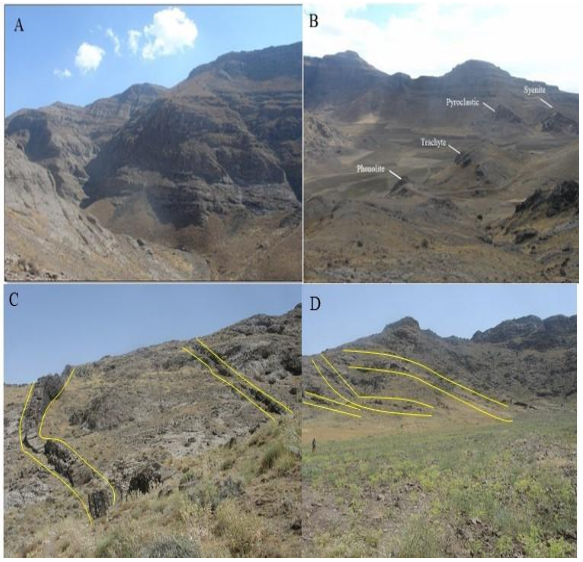

Figure 1: A) Lava and pyroclastic sequence, viewed toward the southeast. B) Intrusion of the syenite mass within the lava and pyroclastic sequence, viewed toward the southeast. C) View of dykes intruding into the pyroclastic sequence, viewed toward east. D) Another view of the dykes intruding the pyroclastic sequence, viewed toward southwest.

Figure 2: Close-up images of xenoliths: A and B) Xenoliths within trachytic lava. C and D) Xenoliths within leucitite lava.

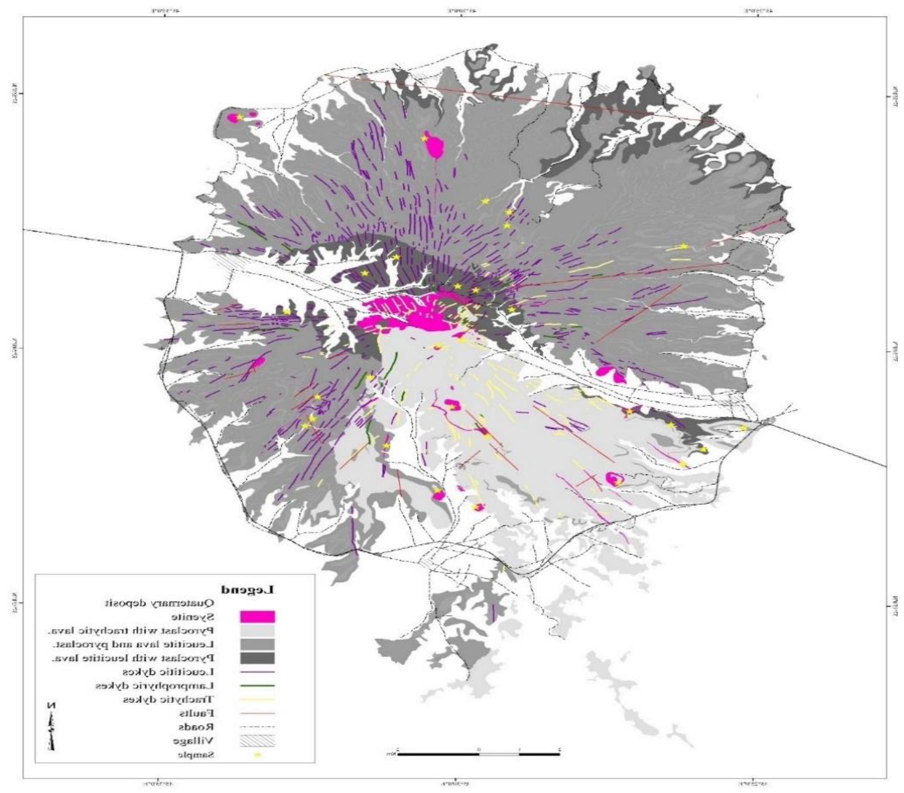

Figure 3: Geological map of the Islamic Island showing sampling locations.

Research methods

After preliminary investigations, 20 samples of lavas and their associated xenoliths were selected, and thin sections were prepared. Following a detailed examination of the thin sections, six suitable samples were chosen for mineral chemistry studies and sent to Canada for further analysis. Quantitative analyses were performed using a Cameca Camebax MBX four-electron microprobe spectrometer equipped with wavelength-dispersive X-ray (WDX) capabilities. The analyses were conducted with an accelerating voltage of 20 kV, a beam current of approximately 20 nA, and a non-concentric electron beam (raster, approximately 7 μm). Additionally, 10 samples of clinopyroxenite xenoliths and 10 samples of host rocks were selected for X-ray fluorescence (XRF) and inductively coupled plasma mass spectrometry (ICP-MS) analysis. These analyses were carried out at the Geological Organization of Tehran Center.

Lithography

Xenoliths on Islamic Island are present in most lava flows, varying in size. This research focuses on examining xenoliths embedded within trachytic and leucitite host rocks.

Trachytes: Trachyte host rocks are light gray, with white sanidine minerals visible to the naked eye (Figure 2-A and B). Most of the xenoliths in the study area are found within trachytic host rocks (Figure 4-A and B). The primary minerals in trachytic host rocks include sanidine, biotite, and opaques. Sanidine minerals are observed in varying sizes (Figure 4-C to F) and make up approximately 40–60% of the rock mass. Biotite constitutes 20–30%, while in some samples, pyroxene minerals account for 10–15%. Additionally, small apatite crystals can be observed within biotite-shaped phenocrysts (Figure 4-A and B).

Leucitites: Leucitite host rocks are gray, with white leucite minerals and black pyroxene minerals that are often visible to the naked eye (Figure 2-C and D). The primary minerals in leucite host rocks include leucite and clinopyroxene, which are commonly embedded in a fine-grained matrix composed of leucite, clinopyroxene, olivine, and opaque minerals. Leucite accounts for approximately 30–40% of the rock matrix, clinopyroxene constitutes 40–50%, and in some samples, olivine makes up 10–15%. Optical properties indicate that the pyroxenes in both xenoliths and their host rocks are of the clinopyroxene type. In leucitite host rocks, most clinopyroxenes exhibit features such as fluctuating zonation, Carlsbad twinning, and sieve texture (Figure 5-A and B). Olivine in leucites appears amorphous and is strongly altered to iddingsite (Figure 5-C). Iddingsite, a reddish pseudo-mineral containing trivalent iron oxide, typically forms in lavas. The formation of iddingsite in olivine occurs uniformly, with oxygen atoms needed for iron oxide production derived from the olivine itself. Leucite minerals are also distinctly visible in the leucitite host rock (Figure 5-D). Petrographic studies reveal that the boundary between the host rock and accompanying xenoliths is sharp, with no reactive margins (Figure 5-E).

Xenoliths in Trachytes: Xenoliths in trachytic host rocks contain clinopyroxene and biotite minerals. The biotite in these xenoliths is euhedral and ranges in color from brown to dark brown. The color of biotite is influenced by its titanium content, with low-titanium biotite appearing green to green-brown, and higher iron content resulting in a browner hue. As titanium increases in iron-rich biotite, its color transitions to reddish-brown (Shelly, 1993). Clinopyroxenes in xenoliths within trachytic host rocks are less abundant than biotite minerals (Figure 6-A and B). Apatite inclusions are occasionally observed within some biotite minerals (Figure 4-A).

Xenoliths in leuisites: Xenoliths in leucitite host rocks contain clinopyroxene and biotite minerals. In some biotite crystals within the host rock, features such as leucite inclusions, zoning, chloritization, and kink bands are observed (Figure 5-F). The clinopyroxenite xenoliths found in both trachytic and leucitite host rocks are predominantly composed of clinopyroxene, biotite, and apatite minerals (Figure 6-A to C). These xenoliths exhibit variability in their mineral arrangements and textures. For instance, in some xenoliths within leucite host rocks, the clinopyroxene and biotite crystals are elongated and oriented (Figure 6-D).

Mineral abbreviations follow the conventions of Whitney and Evans (2010).

Figure 4: A and B) Biotite and clinopyroxene minerals in a xenolith, with apatite mineral observed as an inclusion within biotite. Host rock: trachyte. (Image A captured under PPL light; Image B captured under XPL light). C) Amphibole minerals displaying burnt and oxidized edges within the trachyte matrix. (Image captured under XPL light). D) Sanidine phenocrysts embedded in the trachyte matrix. (Image captured under XPL light). E and F) Biotite minerals and clinopyroxene phenocrysts within the trachyte matrix. (Image E captured under PPL light; Image F captured under XPL light).

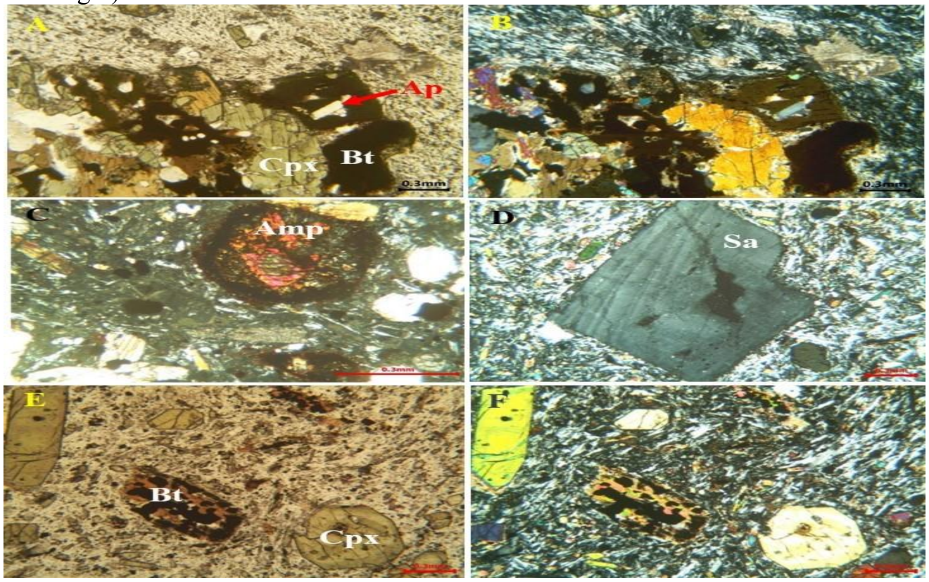

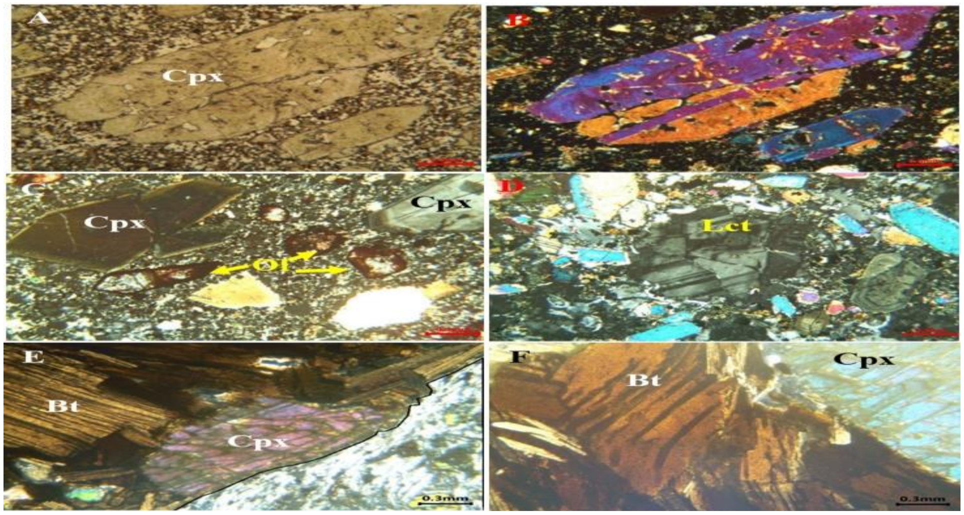

Figure 5: A and B) Clinopyroxene mineral exhibiting a sieve texture. (Image A captured under PPL light; Image B captured under XPL light). C) Idenzitized olivine crystals in leucitite rock. (Image captured under XPL light). D)

Leucite phenocryst associated with clinopyroxene in leucitite rock. (Image captured under XPL light). E) Sharp boundary (outlined with a black line) between xenolith and host rock, without a reaction margin. (Image captured under XPL light). F) Kink bands observed in biotite within a xenolith sample. (Image captured under XPL light).

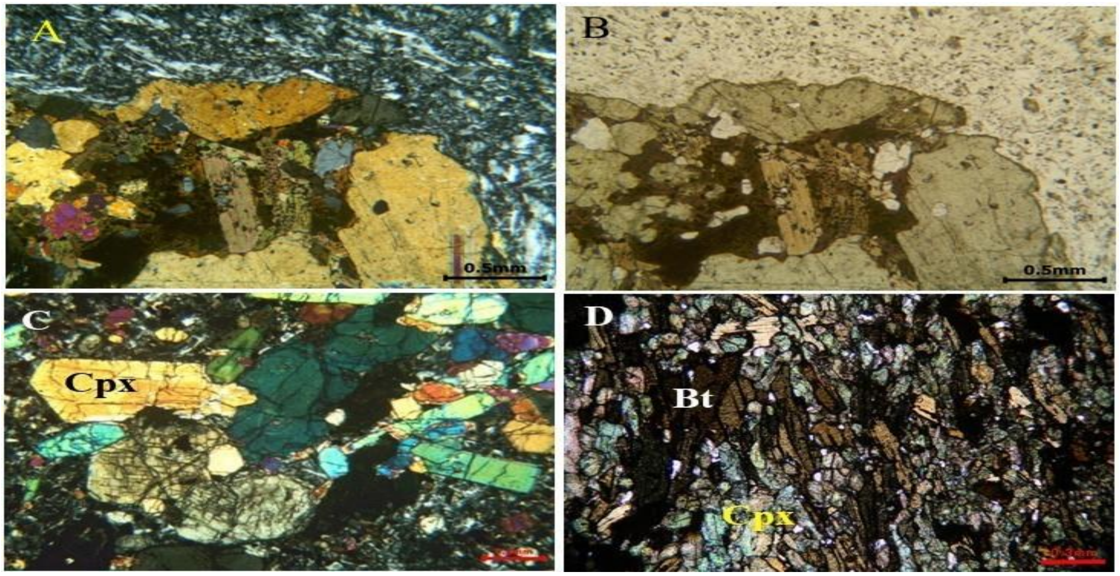

Figure 6: A and B) Biotite, clinopyroxene, and apatite minerals in a xenolith. (Image A captured under PPL light; Image B captured under XPL light). C) Xenolith containing clinopyroxene minerals. (Image captured under XPL light). D) Clinopyroxene and biotite minerals oriented adjacent to each other. (Image captured under XPL light).

Mineral chemistry of clinopyroxene in leucitite , trachytic host rocks and clinopyroxenite xenoliths

The results of spot analyses of clinopyroxene minerals are presented in Table 1. Clinopyroxenes are simple chain silicates, with their basic structural unit consisting of tetrahedra (SiO_4) interconnected by shared oxygen atoms. These connections form long, simple chains of SiO_4 tetrahedra. The base group of clinopyroxenes has a Si_2O_6 structure, characterized by an oxygen-to-silicon ratio of 3:1. The structural formula of pyroxenes is calculated based on 6 oxygen atoms and four cations.

Trachytic host rock and associated xenoliths: To name the clinopyroxenes in the trachytic host rock and associated xenoliths, the method of Morimoto et al. (1988) was applied. These clinopyroxenes are classified within the range of calcium pyroxenes, or Quad (Figure 7-A). For precise naming, the triangular diagram of wollastonite-enstatite-ferrosilicate was utilized. This diagram indicates that the composition of most clinopyroxenes in the trachytic host rock falls outside the diopside range, leaning toward wollastonite and within the fassaite range. Similarly, all pyroxene minerals in the xenoliths from the trachytic host rock are also classified within the fassaite range (Figure 7-B).

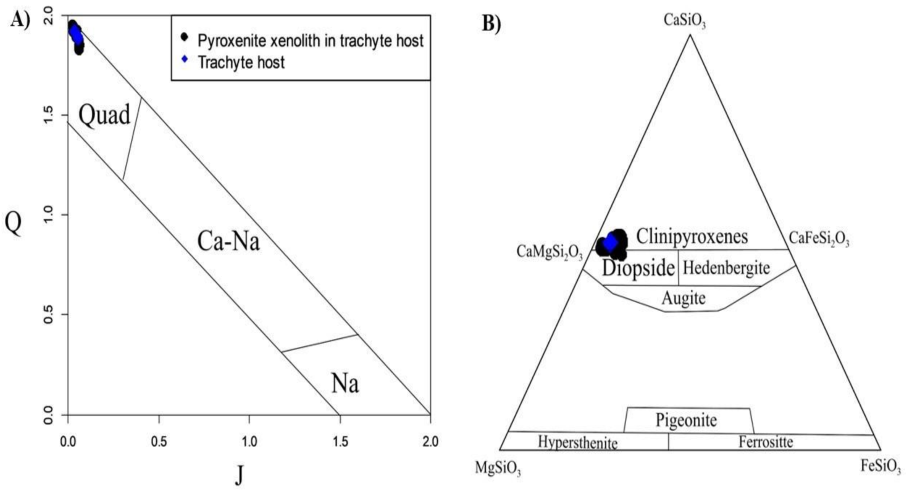

Figure 7: Composition of clinopyroxenes in the trachyte host rock and associated xenoliths: A) Plotted on the J = (2Na), Q = (Ca + Mg + Fe^{2+}) diagram (Morimoto et al., 1988). B) Plotted on the triangular diagram of enstatite (En), wollastonite (Wo), and ferrosilite (Fs) (Morimoto, rt al., 1988).

Luisitite host rock and accompanying xenoliths: The method of Morimoto et al. (1988) has been used to name the clinopyroxenes in the leucitite host rock and its associated xenoliths. Both are placed in the range of calcium pyroxenes, or Quad (Figure 8-A). For precise classification, the triangular diagram of wollastonite-enstatite-ferrosilite has been used. It shows that the composition of clinopyroxenes in the leucitite host rock and its associated xenoliths falls outside the diopside range, inclining toward wollastonite and positioning within the fassaite range (Figure 8-B).

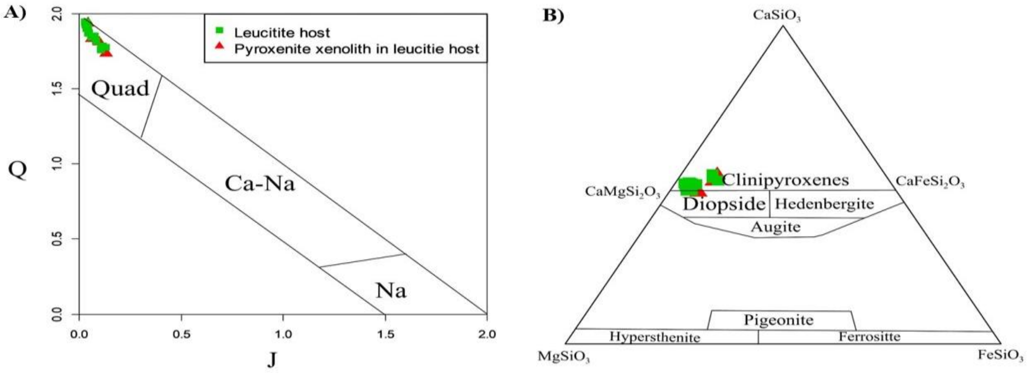

Figure 8: Composition of clinopyroxenes in the leucitite host rock and associated xenoliths: A) On the J = (2Na), Q = (Ca + Mg + Fe^{2+}) diagram (Morimoto et al., 1988). B) On the triangular diagram of enstatite (En), wollastonite (Wo), and ferrosilite (Fr) (Morimoto et al., 1988)

Determination of tectonic environment of clinopyroxenes of host rocks and associated xenoliths

The placement of cations in the cationic positions is such that Al occupies the tetrahedral position

https://doi.org/10.5281/zenodo.15010171

and the M1 position, while Fe^{2+} and Fe^{3+} are found in the M1 position. Mg is distributed between both the M1 and M2 positions, whereas Na and Ca are exclusively in the M2 cation position. Based on the Ca vs. Ti+Cr diagram (Leterrier et al., 1982), the host rocks and accompanying xenoliths are situated within the volcanic arc range (Figure 9-A). The geotectonic diagram, constructed using the clinopyroxene data from the host rocks and associated xenoliths, indicates that the rocks of the studied area belong to a volcanic arc environment (Nisbet and Pearce, 1977) (Figure 9-B).
The values of F1 and F2 are calculated using the following formulas:

$$F1 = -(0.012 * SiO_2) - (0.0807 * TiO_2) + (0.0026 * Al_2O_3) - (0.0012 * FeO\ total) - (0.0026 * MnO) + (0.0087 * MgO) - (0.0128 * CaO) - (0.0419 * Na_2O)$$

$$F2 = -(0.0469 * SiO_2) - (0.0818 * TiO_2) - (0.0212 * Al_2O_3) - (0.0041 * FeO\ total) - (0.1435 * MnO) - (0.0029 * MgO) + (0.0085 * CaO) + (0.016 * Na_2O)$$

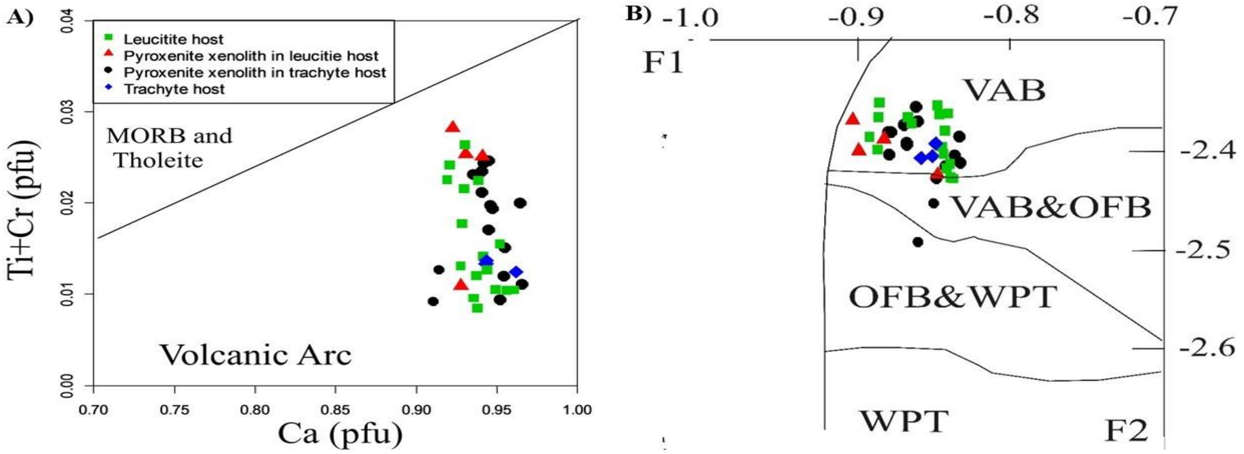

Figure 9: A) Ca vs. Ti+Cr diagram (Leterrier et al., 1982) illustrates the classification of host rocks and associated xenoliths within the volcanic arc field. B) F1 and F2 geotectonic discrimination diagrams (Nisbet and Pearce, 1977) confirm that the studied rocks belong to a volcanic arc environment, distinguishing them from ocean floor basalt (OFB) and within-plate tholeiite (WPT).

Determination of fugacity of clinopyroxenes of host rocks and associated xenoliths

The position of clinopyroxenes on the $Na+Al^{IV}$ vs. $Cr+2Ti+Al^{VI}$ diagram indicates that most of the clinopyroxenes in the xenoliths and their host rocks formed under conditions of high oxygen fugacity (above the line = 0 Fe^{3+}) (Schweitzer et al., 1979). This is significant because oxygen fugacity is directly proportional to pressure. As the ratio of $Na+Al^{IV}$ increases relative to $Cr+2Ti+Al^{VI}$, oxygen fugacity also rises (Figure 10-A). The distribution of aluminum in octahedral (Al^{VI}) and tetrahedral (Al^{IV}) positions provides a reliable method for estimating magma water content and crystallization pressure (Helz, 1973). According to this method, an increase in Al^{IV} corresponds to a decrease in water content within the pyroxene crystallization environment. The Al^{VI} vs. Al^{IV} diagram shows that pyroxenes in the host volcanic rocks and associated xenoliths crystallized at pressures around 5 kbar, with a water content exceeding 10% (Figure 10-B). Based on the Al^{IV} vs. Al^{VI} diagram (Aoki and Shiba, 1973), pyroxenes in the xenoliths of trachytic and leucite host rocks were formed under medium to high-pressure conditions. In contrast, pyroxenes in the trachytic and leucitite host rocks crystallized under low to medium pressures. This variation suggests that the crystallization of pyroxenes occurred during the ascent of magma from deeper levels to the surface (Figure 10-C).

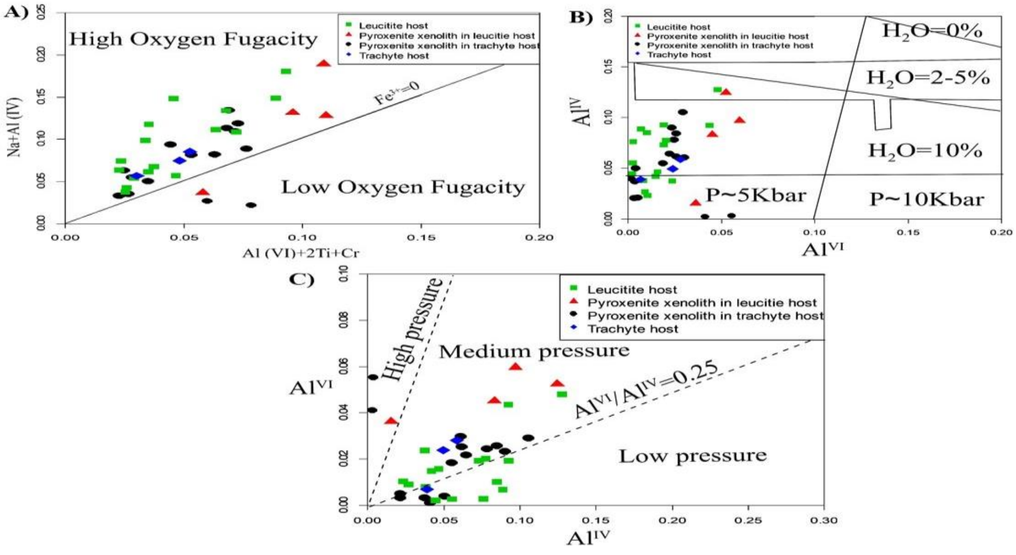

Figure 10: A) Na+Al^{IV} vs. Cr+2Ti+Al^{VI} diagram showing the formation of clinopyroxenes in a high oxygen fugacity environment (above the line = 0 Fe^{3+}) (Schweitzer et al., 1979). B) Al^{VI} vs. Al^{IV} diagram illustrating that the pyroxenes in the host volcanic rocks and associated xenoliths crystallized at approximately 5 kbar pressure, with water content exceeding 10% (Helz, 1973). C) Al^{IV} vs. Al^{VI} diagram demonstrating the pressure conditions for clinopyroxenes, indicating medium to high pressures for xenoliths and low to medium pressures for the host rocks (Aoki and Shiba, 1973).

Table 1- Results of spot analyses of pyroxene minerals

Type	**A-1-Area1-P1**	**A-1-Area1-P2**	**A-1-Area1-P3**	**A-4-Area1-P1**	**A-4-Area1-P2**	**A-4-Area1-P3**	**A-4-Area1-P4**	**A-4-Area1-P5**	**A-4-Area2-P1**	**A-4-Area2-P2**	**A-4-Area2-P3**	**A-4-Area2-P4**	**A-4-Area2-P5**
NAME	Pyroxenite xenolith in trachyte host	Pyroxenite xenolith in trachyte host	Pyroxenite xenolith in trachyte host	Pyroxenite xenolith in trachyte host	Pyroxenite xenolith in trachyte host	Pyroxenite xenolith in trachyte host	Pyroxenite xenolith in trachyte host	Pyroxenite xenolith in trachyte host	Pyroxenite xenolith in trachyte host	Pyroxenite xenolith in trachyte host	Pyroxenite xenolith in trachyte host	Pyroxenite xenolith in trachyte host	Pyroxenite xenolith in trachyte host
Symbol	**19**	**19**	**19**	**19**	**19**	**19**	**19**	**19**	**19**	**19**	**19**	**19**	**19**
Color	**1**	**1**	**1**	**1**	**1**	**1**	**1**	**1**	**1**	**1**	**1**	**1**	**1**
Size	**1.75**	**1.75**	**1.75**	**1.75**	**1.75**	**1.75**	**1.75**	**1.75**	**1.75**	**1.75**	**1.75**	**1.75**	**1.75**
SiO_2	**52.00178**	**52.04242**	**53.80306**	**50.30532**	**51.91407**	**50.9685**	**50.88079**	**50.72248**	**51.5076**	**54.18599**	**52.91953**	**53.50355**	**53.73888**
TiO_2	**0.39866**	**0.62717**	**0.29023**	**0.70557**	**0.61216**	**0.84068**	**0.75561**	**0.88405**	**0.829**	**0.29524**	**0.30191**	**0.27189**	**0.25354**
Al_2O_3	**1.97823**	**2.00279**	**0.60651**	**3.06843**	**1.68348**	**2.34289**	**2.51861**	**2.59229**	**2.06703**	**0.56494**	**1.24891**	**0.96739**	**0.94471**
Fe_2O_3													
Cr_2O_3		**0.08915**	**0.04823**							**0.24408**	**0.12569**	**0.41508**	**0.60654**
FeO	**5.36976**	**4.38175**	**3.12357**	**6.82863**	**5.93967**	**6.25872**	**6.6318**	**6.57648**	**6.04388**	**2.47133**	**3.20462**	**2.96662**	**2.4546**
MnO	**0.10846**	**0.11492**	**0.07876**	**0.16269**	**0.16269**	**0.14978**	**0.14074**	**0.16657**	**0.16657**	**0.06843**	**0.06456**	**0.06327**	**0.05552**
MgO	**14.74359**	**15.41352**	**17.06349**	**14.004**	**14.82981**	**14.47163**	**14.30912**	**14.32405**	**14.66233**	**17.39514**	**16.90762**	**17.15635**	**17.46645**
CaO	**24.34987**	**24.38485**	**24.25193**	**23.68806**	**23.73983**	**23.57892**	**23.58452**	**23.71884**	**23.46979**	**24.50098**	**24.27012**	**24.22814**	**24.15818**
Na_2O	**0.41247**	**0.28846**	**0.16715**	**0.40304**	**0.36799**	**0.43674**	**0.3963**	**0.40169**	**0.39226**	**0.20354**	**0.18602**	**0.20354**	**0.18467**
Totals	**99.36282**	**99.34503**	**99.43293**	**99.16574**	**99.2497**	**99.04786**	**99.21749**	**99.38645**	**99.13846**	**99.92967**	**99.22898**	**99.77583**	**99.86309**
Si	**1.924483**	**1.920888**	**1.970808**	**1.874616**	**1.927716**	**1.898132**	**1.89407**	**1.885065**	**1.916052**	**1.970934**	**1.94159**	**1.951951**	**1.95586**
Ti	**0.011099**	**0.017415**	**0.007998**	**0.01978**	**0.017101**	**0.023553**	**0.021161**	**0.024717**	**0.0232**	**0.008079**	**0.008333**	**0.007462**	**0.006942**
Al	**0.086283**	**0.087123**	**0.026184**	**0.134763**	**0.073675**	**0.102833**	**0.110499**	**0.113544**	**0.090623**	**0.024218**	**0.054004**	**0.041595**	**0.040523**

Fe3	**0.072147**	**0.054312**	**0.026679**	**0.105565**	**0.063184**	**0.085332**	**0.087641**	**0.095835**	**0.059164**	**0.02509**	**0.055736**	**0.042003**	**0.029451**
Cr^{3+}	**0**	**0.002602**	**0.001397**	**0**	**0**	**0**	**0**	**0**	**0**	**0.007019**	**0.003646**	**0.011973**	**0.017453**
Fe^{2+}	**0.094048**	**0.080946**	**0.069009**	**0.107249**	**0.12127**	**0.109598**	**0.118822**	**0.108568**	**0.128863**	**0.050087**	**0.042594**	**0.048511**	**0.045263**
Mn	**0.0034**	**0.003593**	**0.002444**	**0.005135**	**0.005117**	**0.004725**	**0.004438**	**0.005243**	**0.005248**	**0.002108**	**0.002006**	**0.001955**	**0.001712**
Mg	**0.813411**	**0.84812**	**0.931785**	**0.777967**	**0.820927**	**0.803438**	**0.794083**	**0.793601**	**0.813111**	**0.943243**	**0.924772**	**0.933086**	**0.947686**
Ca	**0.965532**	**0.964359**	**0.951826**	**0.945806**	**0.944517**	**0.940854**	**0.940683**	**0.944481**	**0.935447**	**0.954867**	**0.954086**	**0.947066**	**0.942079**
Na	**0.029596**	**0.020643**	**0.011871**	**0.02912**	**0.026493**	**0.031535**	**0.028603**	**0.028944**	**0.028291**	**0.014354**	**0.013233**	**0.014397**	**0.013031**

Type	**96-SP-26-Area3-P1**	**96-SP-26-Area3-P2**	**96-SP-26-Area3-P3**	**96-SP-26-Area3-P4**	**T4a-Area2-P4**	**T4a-Area2-P5**	**J-1-Area1-P1**	**J-1-Area1-P2**	**J-1-Area1-P3**	**J-1-Area1-P4**	**J-1-Area1-P5**	**J-1-Area1-P6**	**J-1-Area1-P7**
NAME	Pyroxenite xenolith in leucitie host	Pyroxenite xenolith in leucitie host	Pyroxenite xenolith in leucitie host	Pyroxenite xenolith in leucitie host	Pyroxenite xenolith in trachyte host	Pyroxenite xenolith in trachyte host	Leucitite host	Leucitite host	Leucitite host	Leucitite host	Leucitite host	Leucitite host	Leucitite host
Symbol	**19**	**19**	**19**	**19**	**19**	**19**	**15**	**15**	**15**	**15**	**15**	**15**	**15**
Color	**1**	**1**	**1**	**1**	**1**	**1**	**1**	**1**	**1**	**1**	**1**	**1**	**1**
Size	**1.75**	**1.75**	**1.75**	**1.75**	**1.75**	**1.75**	**1.5**	**1.5**	**1.5**	**1.5**	**1.5**	**1.5**	**1.5**
SiO_2	**50.3695**	**49.28916**	**50.65189**	**53.29818**	**54.79568**	**53.6854**	**50.47432**	**53.02436**	**50.9792**	**51.38994**	**52.70774**	**51.30651**	**52.32909**
TiO_2	**0.89572**	**1.00081**	**0.90407**	**0.39198**	**0.3703**	**0.33194**	**0.86236**	**0.38031**	**0.76896**	**0.55712**	**0.3753**	**0.9491**	**0.37697**
Al_2O_3	**3.56913**	**4.00747**	**2.91727**	**1.18278**	**1.13932**	**0.99951**	**2.54884**	**1.05997**	**2.22385**	**1.8044**	**1.07319**	**2.11238**	**1.15066**
Fe_2O_3													
Cr_2O_3					**0.09062**								
FeO	**7.13739**	**8.90887**	**7.89512**	**4.07042**	**3.96364**	**5.19738**	**5.85348**	**3.77968**	**5.74413**	**4.84102**	**3.5867**	**5.80845**	**3.84143**
MnO	**0.17948**	**0.27116**	**0.25566**	**0.11621**	**0.1033**	**0.2053**	**0.15107**	**0.06843**	**0.13816**	**0.09555**	**0.07747**	**0.13429**	**0.06973**
MgO	**13.31914**	**12.03233**	**12.9593**	**16.03371**	**16.30069**	**15.51634**	**14.94921**	**16.55275**	**14.98238**	**15.70869**	**16.54777**	**15.04373**	**16.41843**
CaO	**23.56074**	**22.97588**	**23.25991**	**23.38444**	**23.40822**	**22.9381**	**23.03884**	**24.07563**	**23.26411**	**23.92452**	**24.18057**	**23.43621**	**24.25193**
Na2O	**0.42595**	**0.89369**	**0.66724**	**0.29655**	**0.26959**	**0.34373**	**0.57019**	**0.22511**	**0.47178**	**0.31407**	**0.2615**	**0.49874**	**0.26555**
Totals	**99.45705**	**99.37937**	**99.51046**	**98.77427**	**100.4414**	**99.2177**	**98.44831**	**99.16624**	**98.57257**	**98.63531**	**98.81024**	**99.28941**	**98.70379**
Si	**1.877763**	**1.847191**	**1.891327**	**1.973595**	**1.996288**	**1.988191**	**1.8829**	**1.951444**	**1.900861**	**1.908168**	**1.944855**	**1.900486**	**1.93424**
Ti	**0.025121**	**0.028217**	**0.025396**	**0.01092**	**0.010149**	**0.009248**	**0.024201**	**0.01053**	**0.02157**	**0.015563**	**0.010418**	**0.026448**	**0.010483**
Al	**0.156816**	**0.177005**	**0.128381**	**0.051618**	**0.048919**	**0.043626**	**0.112061**	**0.045976**	**0.097728**	**0.078963**	**0.046671**	**0.092219**	**0.050127**
Fe^{3+}	**0.068204**	**0.137116**	**0.086477**	**0.000644**	**0**	**0**	**0.114977**	**0.04614**	**0.091516**	**0.096186**	**0.061491**	**0.089732**	**0.079459**
Cr^{3+}	**0**	**0**	**0**	**0**	**0.00261**	**0**	**0**	**0**	**0**	**0**	**0**	**0**	**0**
Fe^{2+}	**0.154322**	**0.142107**	**0.160069**	**0.125409**	**0.120765**	**0.160974**	**0.067639**	**0.070194**	**0.087606**	**0.054143**	**0.049191**	**0.090205**	**0.039289**
Mn	**0.005667**	**0.008607**	**0.008086**	**0.003645**	**0.003188**	**0.00644**	**0.004773**	**0.002133**	**0.004363**	**0.003005**	**0.002421**	**0.004213**	**0.002183**
Mg	**0.740219**	**0.672234**	**0.721379**	**0.885096**	**0.885306**	**0.856647**	**0.831353**	**0.908158**	**0.832816**	**0.869539**	**0.910255**	**0.830727**	**0.90471**
Ca	**0.941101**	**0.922585**	**0.930579**	**0.927783**	**0.913733**	**0.910193**	**0.920855**	**0.949363**	**0.929433**	**0.951822**	**0.95599**	**0.930151**	**0.960478**
Na	**0.030788**	**0.064937**	**0.048306**	**0.021291**	**0.019043**	**0.024681**	**0.04124**	**0.016063**	**0.034107**	**0.02261**	**0.018708**	**0.035819**	**0.019031**

Type	**J-1-Area2-Px-P1**	**J-1-Area2-Px-P2**	**J-1-Area2-Px-P3**	**T-5-Area2-P1**	**T-5-Area2-P2**	**T-5-Area2-P3**	**96-SP-26-Area2-P1**	**96-SP-26-Area2-P2**	**96-SP-26-Area2-P3**	**96-SP-26-Area2-P4**	**96-SP-26-Area2-P5**	**96-SP-26-Area2-P6**
NAME	Leucitite host	Leucitite host	Leucitite host	Trachyte host	Trachyte host	Trachyte host	Leucitite host	Leucitite host	Leucitite host	Leucitite host	Leucitite host	Leucitite host
Symbol	**15**	**15**	**15**	**15**	**15**	**15**	**15**	**15**	**15**	**15**	**15**	**15**
Color	**1**	**1**	**1**	**1**	**1**	**1**	**1**	**1**	**1**	**1**	**1**	**1**
Size	**1.5**	**1.5**	**1.5**	**1.5**	**1.5**	**1.5**	**2**	**2**	**2**	**2**	**2**	**2**
SiO_2	**53.91002**	**54.01698**	**51.25731**	**53.234**	**52.89172**	**52.42963**	**49.64856**	**53.04575**	**53.44365**	**50.38448**	**50.54706**	**53.10779**
TiO_2	**0.26688**	**0.23185**	**0.50875**	**0.39866**	**0.38031**	**0.407**	**0.80232**	**0.3286**	**0.29857**	**0.80232**	**0.62884**	**0.35362**

Al_2O_3	0.82946	0.77844	2.19173	1.06375	1.6967	2.0009	3.99803	1.44352	1.31882	3.07976	2.15206	1.41518
Fe_2O_3												
Cr_2O_3	0.07892	0.07308		0.04969	0.11108	0.07015		0.12423	0.133			0.11546
FeO	3.4156	3.36414	5.48941	4.05627	4.10515	4.29427	8.25791	3.92376	3.70892	8.67987	8.6966	4.10901
MnO	0.07876	0.08393	0.15624	0.09297	0.09297	0.09297	0.16657	0.08651	0.08651	0.25695	0.31764	0.08909
MgO	17.11821	17.10826	15.36875	16.21446	16.00884	15.76176	12.56463	16.34878	16.71028	12.56961	12.78021	16.36536
CaO	23.93991	23.99028	23.74263	24.50798	24.00987	23.91752	23.50896	24.02806	23.97489	22.9325	23.08361	23.54535
Na_2O	0.22646	0.20085	0.40439	0.24668	0.35451	0.37204	0.73329	0.29251	0.27633	0.77777	0.87213	0.27229
Totals	99.86422	99.84781	99.11921	99.86446	99.65115	99.34624	99.68027	99.62172	99.95097	99.48326	99.07815	99.37315
Si	1.966032	1.970531	1.896999	1.94983	1.939991	1.929961	1.84992	1.944285	1.949826	1.885082	1.897146	1.952536
Ti	0.007322	0.006363	0.014165	0.010985	0.010494	0.011271	0.02249	0.009061	0.008195	0.022583	0.017756	0.009781
Al	0.035651	0.033468	0.095599	0.04592	0.073345	0.086806	0.175569	0.062357	0.056707	0.135802	0.095195	0.061321
Fe^{3+}	0.031379	0.024842	0.111091	0.048529	0.047674	0.05524	0.132586	0.048138	0.042962	0.105288	0.138466	0.0301
Cr^{3+}	0.002276	0.002108	0	0.001439	0.003221	0.002042	0	0.0036	0.003836	0	0	0.003356
Fe^{2+}	0.072795	0.077793	0.058814	0.075723	0.07825	0.07696	0.12474	0.072139	0.070204	0.166302	0.134509	0.096242
Mn	0.002433	0.002593	0.004898	0.002884	0.002888	0.002899	0.005257	0.002686	0.002673	0.008143	0.010098	0.002774
Mg	0.930658	0.930399	0.847931	0.885362	0.875352	0.864942	0.697922	0.893317	0.908854	0.701077	0.715078	0.896968
Ca	0.935444	0.937697	0.941487	0.96181	0.943574	0.943326	0.938542	0.943631	0.937196	0.919303	0.928288	0.927513
Na	0.016012	0.014206	0.029017	0.017518	0.025211	0.026553	0.052974	0.020787	0.019547	0.056419	0.063464	0.01941

Mineral chemistry of mica in host rocks of leucite, trachyte and pyroxenite xenoliths

The results of the spot analysis of biotite minerals are presented in Table 2. Biotite minerals belong to a solid-solution series comprising four end members: annite $KFe_3AlSi_3O_{10}(OH)_2$, phlogopite $KMg_3AlSi_3O10(OH)_2$, siderophyllite $KFe_3Al[Al2Si_2O_{10}](OH)_2$, and eastonite $KMg_2Al[Al_2Si_2O_{10}](OH)_2$. The substitution mechanisms represented on the horizontal and vertical axes include Mg-Fe exchange and the (Mg, Fe) Si ↔ ^{VI}Al exchange (Chermak substitution), respectively. The nomenclature of micas was determined using the method of Speer (1984) and the Al^{IV} versus $Fe^{2+}/(Fe^{2+}+Mg)$ diagram (Figure 11-A). According to this diagram, the micas in the trachytic host rock and associated xenoliths belong to the biotite and phlogopite types, while the micas in the leucitite host rock and associated xenoliths fall within the phlogopite range (Figure 11-A). To determine the origin of the micas, the triangular diagram of MgO, FeO+MnO, and $10TiO_2$ was employed (Nachit et al., 2005) (Figure 11-B). Based on this diagram, the micas in the leucitite host rock and its xenoliths are identified as primary biotites. In contrast, the micas in the trachytic host rock and its associated xenoliths range between primary biotites and recrystallized primary biotites (Figure 11-B).

https://doi.org/10.5281/zenodo.15010171

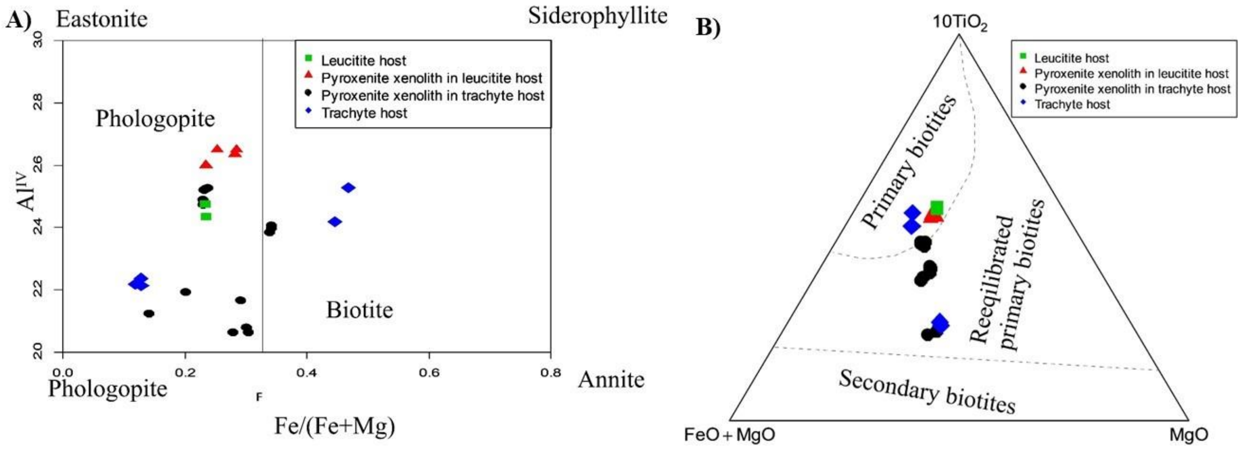

Figure 11: A) $Fe^{2+}/(Fe^{2+}+Mg)$ versus Al^{IV} plot, illustrating mica classification based on Speer (1984). B) Triangular plot of MgO, FeO+MnO, and $10TiO_2$, used to determine the origin of micas (Nachit et al., 2005).

Table 2- Results of spot analyses of biotite minerals

Type	96-SP-26-Area1-BioA-P1	96-SP-26-Area1-BioA-P2	96-SP-26-Area1-BioB-P1	96-SP-26-Area1-BioB-P2	A-1-Area3-BioA-P1	A-1-Area3-BioA-P2	A-1-Area3-BioA-P3	A-1-Area3-BioB-P1	A-1-Area3-BioB-P2	A-1-Area3-BioB-P3	A-3-Area1-P1	A-3-Area1-P2	A-3-Area1-P3
Name	Pyroxenite xenolith in leucitite host	Pyroxenite xenolith in leucitite host	Pyroxenite xenolith in leucitite host	Pyroxenite xenolith in leucitite host	Pyroxenite xenolith in trachyte host	Pyroxenite xenolith in trachyte host	Pyroxenite xenolith in trachyte host	Pyroxenite xenolith in trachyte host	Pyroxenite xenolith in trachyte host	Pyroxenite xenolith in trachyte host	Pyroxenite xenolith in trachyte host	Pyroxenite xenolith in trachyte host	Pyroxenite xenolith in trachyte host
SiO_2	35.45867	35.56136	35.5635	36.44703	36.08976	36.2716	36.7508	36.59678	36.28872	36.17962	37.41612	38.9179	39.38213
TiO_2	4.93233	5.05909	5.04575	5.01239	2.98241	3.06748	2.94905	3.01244	3.14088	3.13587	4.0316	1.44117	1.56794
Al_2O_3	15.0285	15.10785	15.12297	15.225	14.1518	14.43333	14.52591	14.69974	14.48245	14.56181	11.54439	12.58925	12.2038
FeO	11.68123	11.47539	10.28926	9.61901	9.79654	9.77595	9.83771	10.05641	10.09886	10.17605	12.97672	9.14429	6.60607
MnO	0.09813	0.09942	0.10717	0.08006	0.13945	0.11234	0.1317	0.12008	0.14462	0.11621	0.16657	0.13687	0.09813
MgO	16.51958	16.41345	17.08007	17.63559	18.38015	18.47965	18.64381	18.75657	18.61065	18.45975	16.94244	20.50438	22.60705
CaO	0.05737		0.05877	0.03638	0.05457	0.14132				0.06436			
Na2O	0.54323	0.49066	0.60254	0.58232	0.30194	0.51761	0.42595	0.48931	0.52301	0.53244	0.24802	0.30599	0.25072
K2O	9.05981	8.94778	9.28748	9.52599	9.54285	8.90441	9.6067	9.84159	9.61995	9.29591	9.62717	10.32705	10.53665
Cl	0.083	0.07	0.074	0.072			0.036						
F	1.144	1.329	1.332	1.708	0.917	0.615	0.752	0.876	0.728	0.729	1.289	1.699	2.019
TOTAL	92.81513	92.57828	92.58479	93.58905	90.79275	91.05697	92.26091	92.9262	92.26242	91.8753	92.30631	92.72018	92.60577
O=F,Cl	0.500415	0.575376	0.577542	0.735406	0.386105	0.258947	0.324756	0.368842	0.306526	0.306947	0.542737	0.715368	0.850105
Si	5.349733	5.364777	5.350024	5.399901	5.520172	5.509973	5.525732	5.479488	5.473482	5.471976	5.718929	5.805804	5.816006
Al Total	2.650267	2.635223	2.649976	2.600099	2.479828	2.490027	2.474268	2.520512	2.526518	2.528024	2.079491	2.194196	2.123982
Al	0.021849	0.050778	0.031157	0.058244	0.071172	0.093895	0.09966	0.07329	0.047812	0.067504	0	0.019118	0
Ti	0.559698	0.574034	0.570912	0.558548	0.343106	0.350474	0.333501	0.33924	0.356316	0.356722	0.463474	0.161704	0.174159
Fe2	1.473674	1.447585	1.294311	1.191673	1.252981	1.241781	1.236859	1.259051	1.273701	1.286953	1.658533	1.140686	0.815778
Mn	0.012539	0.012702	0.013654	0.010046	0.018064	0.014453	0.016771	0.015227	0.018474	0.014885	0.021562	0.017293	0.012273
Mg	3.715639	3.691459	3.830591	3.895279	4.19124	4.185057	4.179098	4.186734	4.184836	4.162276	3.860618	4.560206	4.977307
Ca	0.009273	0	0.009472	0.005774	0.008942	0.022999	0	0	0	0.010428	0	0	0
Na	0.158892	0.143503	0.17573	0.167261	0.089536	0.152438	0.124162	0.142033	0.152936	0.15612	0.073494	0.088497	0.071783
K	1.743563	1.721859	1.782207	1.800291	1.861897	1.725428	1.842495	1.879626	1.850861	1.793416	1.876997	1.965162	1.984893
Cl	0.021223	0.017897	0.018867	0.018079	0	0	0.009174	0	0	0	0	0	0
F	0.545773	0.633979	0.633624	0.80018	0.443521	0.295416	0.357534	0.414742	0.347216	0.348646	0.622996	0.801462	0.942841
TOTAL	15.69513	15.64192	15.70803	15.68712	15.83694	15.78652	15.83255	15.8952	15.88494	15.84831	15.7531	15.95266	15.97618

https://doi.org/10.5281/zenodo.15010171

Type	A-3-Area2-Bt-P1	A-3-Area2-Bt-P2	A-3-Area2-Bt-P3	J-1-Area2-Bt-P1	J-1-Area2-Bt-P2	T4a-Area1-P3	T4a-Area1-P4	T4a-Area2-P1	T4a-Area2-P2	T4a-Area2-P3	T-5-Area1-P1	T-5-Area1-P2	T-5-Area1-P3
Name	Pyroxenite xenolith in trachyte host	Pyroxenite xenolith in trachyte host	Pyroxenite xenolith in trachyte host	Leucitite host	Leucitite host	Trachyte host	Trachyte host	Pyroxenite xenolith in trachyte host	Pyroxenite xenolith in trachyte host	Pyroxenite xenolith in trachyte host	Trachyte host	Trachyte host	Trachyte host
SiO_2	**37.3006**	**37.66428**	**38.3895**	**35.56992**	**35.76245**	**36.16036**	**35.16559**	**37.05886**	**36.80215**	**36.94334**	**39.99182**	**39.56824**	**39.40566**
TiO_2	**3.96154**	**2.78559**	**2.90402**	**5.43773**	**5.58619**	**4.28347**	**4.86894**	**3.81976**	**3.77305**	**3.88648**	**1.68303**	**1.7264**	**1.74975**
Al_2O_3	**11.51605**	**12.16035**	**11.61241**	**13.7947**	**13.60009**	**13.50562**	**13.80982**	**13.80604**	**13.53018**	**13.67378**	**13.47728**	**13.51884**	**13.42248**
FeO	**13.42956**	**13.0732**	**12.49943**	**9.57655**	**9.66532**	**17.56816**	**18.32203**	**14.09081**	**13.90041**	**14.11911**	**5.4804**	**5.84319**	**5.83032**
MnO	**0.15753**	**0.1911**	**0.1614**	**0.04519**	**0.07489**	**0.29311**	**0.26212**	**0.19627**	**0.20401**	**0.20789**			
MgO	**17.35866**	**17.9689**	**18.20106**	**17.7384**	**17.66378**	**12.28936**	**11.7239**	**15.29247**	**15.24604**	**15.33558**	**23.00172**	**22.22565**	**22.45781**
CaO	**0.05037**		**0.07695**	**0.05877**	**0.03638**	**0.15391**							
Na2O	**0.31003**	**0.31003**	**0.27768**	**0.25207**	**0.23994**	**0.44213**	**0.35856**	**0.40034**	**0.41247**	**0.41517**	**0.25072**	**0.23454**	**0.24802**
K2O	**9.64042**	**10.01987**	**9.6862**	**9.2935**	**9.46696**	**9.39107**	**9.20677**	**9.5561**	**9.52237**	**9.61151**	**10.48726**	**10.25477**	**10.42823**
Cl	**0.043**		**0.038**	**0.043**	**0.036**	**0.056**	**0.071**	**0.04**		**0.04**			
F	**1.483**	**1.49**	**1.817**	**0.733**	**0.569**	**0.593**	**0.324**	**0.763**	**0.674**	**0.822**	**0.805**	**0.725**	**0.553**
TOTAL	**93.12104**	**93.5266**	**93.19993**	**91.16311**	**91.48528**	**93.49647**	**93.14201**	**93.61393**	**92.74396**	**93.58614**	**93.72551**	**92.72491**	**92.89555**
O=F,Cl	**0.634125**	**0.627368**	**0.773628**	**0.318335**	**0.247703**	**0.262322**	**0.152444**	**0.33029**	**0.283789**	**0.355132**	**0.338947**	**0.305263**	**0.232842**
Si	**5.671172**	**5.69149**	**5.78631**	**5.416725**	**5.433953**	**5.581519**	**5.472538**	**5.602127**	**5.614898**	**5.593003**	**5.782751**	**5.787155**	**5.763427**
Al Total	**2.063434**	**2.165571**	**2.062727**	**2.47569**	**2.435345**	**2.418481**	**2.527462**	**2.397873**	**2.385102**	**2.406997**	**2.217249**	**2.212845**	**2.236573**
Al	**0**	**0**	**0**	**0**	**0**	**0.038288**	**0.005268**	**0.061702**	**0.047676**	**0.032653**	**0.079405**	**0.117326**	**0.07701**
Ti	**0.453015**	**0.316596**	**0.329216**	**0.622821**	**0.638405**	**0.497287**	**0.569898**	**0.434299**	**0.432965**	**0.442545**	**0.18304**	**0.189912**	**0.192482**
Fe2	**1.707348**	**1.651891**	**1.57537**	**1.219456**	**1.228027**	**2.26751**	**2.384227**	**1.781148**	**1.77337**	**1.78739**	**0.662642**	**0.714614**	**0.713046**
Mn	**0.020284**	**0.024457**	**0.020603**	**0.005828**	**0.009637**	**0.038317**	**0.034547**	**0.025128**	**0.026361**	**0.026655**	**0**	**0**	**0**
Mg	**3.934577**	**4.048021**	**4.089882**	**4.027107**	**4.001263**	**2.827964**	**2.719993**	**3.446382**	**3.467773**	**3.461258**	**4.958479**	**4.84616**	**4.896824**
Ca	**0.008204**	**0**	**0.012426**	**0.009588**	**0.005922**	**0.025451**	**0**	**0**	**0**	**0**	**0**	**0**	**0**
Na	**0.091384**	**0.090826**	**0.081141**	**0.074419**	**0.070681**	**0.132306**	**0.108179**	**0.117327**	**0.122003**	**0.121855**	**0.070285**	**0.066503**	**0.070326**
K	**1.869657**	**1.931379**	**1.862309**	**1.80527**	**1.834882**	**1.849029**	**1.827625**	**1.842683**	**1.853202**	**1.856135**	**1.934347**	**1.913169**	**1.945547**
Cl	**0.01108**	**0**	**0.009707**	**0.011098**	**0.009271**	**0.014649**	**0.018726**	**0.010248**	**0**	**0.010263**	**0**	**0**	**0**
F	**0.712975**	**0.711965**	**0.866005**	**0.352967**	**0.273387**	**0.289435**	**0.159438**	**0.364722**	**0.325166**	**0.393511**	**0.368074**	**0.335299**	**0.255755**
TOTAL	**15.81908**	**15.92023**	**15.81998**	**15.6569**	**15.65812**	**15.67615**	**15.64974**	**15.70867**	**15.72335**	**15.72849**	**15.8882**	**15.84768**	**15.89524**

Temperature - pressure measurement

In the pyroxene mineral temperature measurement method by Soesoo (Soesoo, 1997), evaluating the temperature requires calculating two indices, XPY and YPT, based on point analysis data. These two indices are determined as follows:

XpT=(0.446*SiO2) + (0.187*TiO2) - (0.404*Al2O3) +(0.346*FeO) - (0.052*MnO) + (0.309*MgO) +(0.431*CaO) - (0.446*Na2O)
YpT=(-0.369*SiO2) + (0.535*TiO2) - (0.317*Al2O3)+ (0.323*FeO) + (0.235*MnO) - (0.516*MgO) - (0.167*CaO) - (0.153*Na2O)

The value of XPY for the examined samples ranges from 36.8 to 40.65, and the value of YPT ranges from -26.2 to -32.4. This method is preferred due to its advantages, including:

1. No requirement for the presence of two pyroxenes for temperature measurement.
2. Applicability to both Fe-Ca-Mg and Fe-Mg pyroxenes.

Based on this method, the formation temperature of clinopyroxenes in the trachyte and leucite host rock xenoliths is estimated to be 1200–1300°C, while the formation temperature of clinopyroxenes in the trachyte and leucite host rocks themselves is also approximately 1200–1300°C (Figure 12-A).

Additionally, using Soesoo's method (Soesoo, 1997) to evaluate the pressure governing the formation of rocks containing clinopyroxene, the pressure calculated for clinopyroxenes in the trachyte and leucite host rocks is 6–10 kbar. This pressure corresponds to an approximate depth of 20–35 km (Figure 12-B). According to calculations using the formula of Putirka et al. (2003), the average crystallization temperature in pyroxenite xenoliths found in trachytes is $1129^{\circ\mathrm{C}}$, while in pyroxenite xenoliths in leucites, it is $1244–1301^{\circ\mathrm{C}}$. Similarly, the crystallization temperature in the trachyte host rock is estimated to be $1027^{\circ\mathrm{C}}$, and in the leucite host rock, it is $996–1143^{\circ\mathrm{C}}$. The lower crystallization temperatures of pyroxenes in the trachytic and leucitite host rocks compared to the accompanying pyroxenite xenoliths suggest that the pyroxenite xenoliths originated at greater depths. These xenoliths are likely related to differential crystallization at great depths, followed by the production of cumulus phases and subsequent emplacement in new magmatic pulses that transported them to the surface. The average crystallization pressure in pyroxenite xenoliths in trachytes, calculated using the formula of Putirka et al. (2003), is 5.95 kbar, while in pyroxenite xenoliths in leucites, it is 15.65–16.18 kbar. For the trachytic host rock, the crystallization pressure is 2.6 kbar, and for the leucitite host rock, it is 4.83–4.92 kbar. The lower crystallization pressures of pyroxenes in the host rocks compared to their associated xenolith-pyroxenites indicate that the pyroxenite xenoliths originated at greater depths. Furthermore, the depth of formation of pyroxenite xenoliths in leucitite host rock is greater than that of pyroxenite xenoliths in trachyte host rock. Using the formula of Putirka et al. (2008), the average crystallization temperature in pyroxenite xenoliths in trachytes is $1140^{\circ\mathrm{C}}$, while in pyroxenite xenoliths in leucites, it is $1133–1205^{\circ\mathrm{C}}$. Similarly, the crystallization temperature in the trachyte host rock is estimated to be $1111^{\circ\mathrm{C}}$, and in the leucite host rock, it is $1044–1140^{\circ\mathrm{C}}$. These temperatures reinforce the conclusion that the pyroxenite xenoliths in the trachyte and leucitite host rocks formed at greater depths and temperatures before being transported to the surface by new magmatic pulses. According to the same formula, the average crystallization pressure in pyroxenite xenoliths in trachytes is 2.69 kbar, and in pyroxenite xenoliths in leucites, it is 8.66–11.36 kbar. For the trachytic host rock, the crystallization pressure is 10.5 kbar, and for the leucitite host rock, it is 3.36–5.21 kbar. The higher crystallization pressure of pyroxenes in the trachytic host rock compared to their associated xenolith-pyroxenites suggests that some pyroxenite xenoliths in trachyte host rock formed at shallower depths than the trachytic host rock itself. However, the lower crystallization pressure in leucitite host rock compared to its associated xenoliths indicates that the pyroxenite xenoliths in leucitite host rock formed at greater depths.

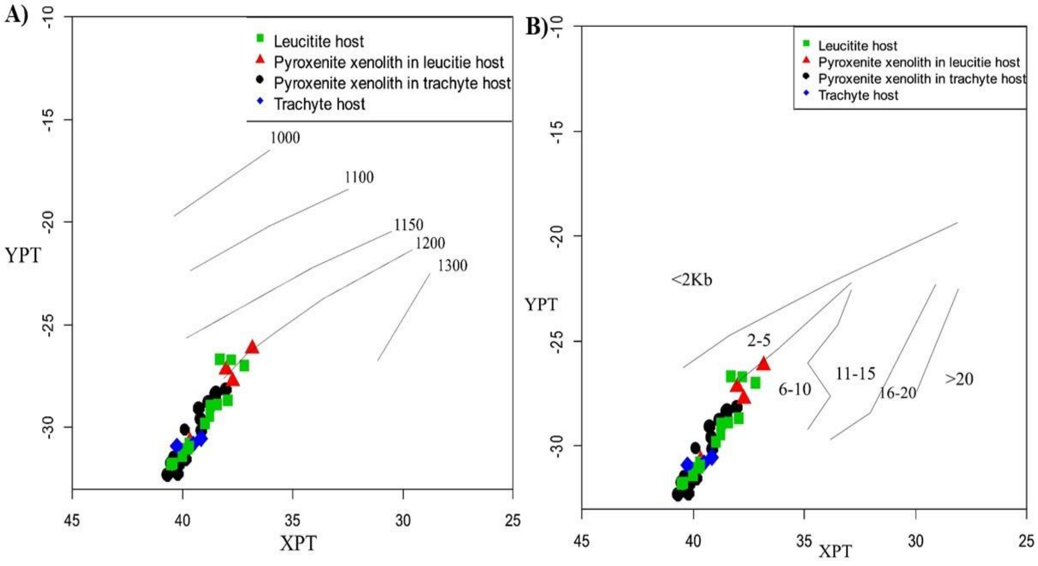

Figure 12: A) Determination of the crystallization temperature of clinopyroxenes in host rocks and associated xenoliths using the Soesoo method (Soesoo, 1997). B) Determination of the crystallization pressure of clinopyroxenes in host rocks and associated xenoliths using the Soesoo method (Soesoo, 1997).

Hole rock geochemistry

The results of the whole-rock analysis are presented in Tables 3 and 4. On the TAS diagram (Le Bas et al., 1986), the volcanic samples of the leucitite and trachytic host rocks from Islamic Island are classified into trachyte, trachydacite, trachyandesite, and phonolite (represented by red triangle symbols) as well as tephrite and basanite (represented by green circle symbols) (Figure 13-A). On the Co-Th diagram (Hastie et al., 2007), all volcanic samples from the leucitite and trachytic host rocks of Islamic Island fall within the calc-alkaline series with high potassium and shoshonitic characteristics (Figure 13-B).

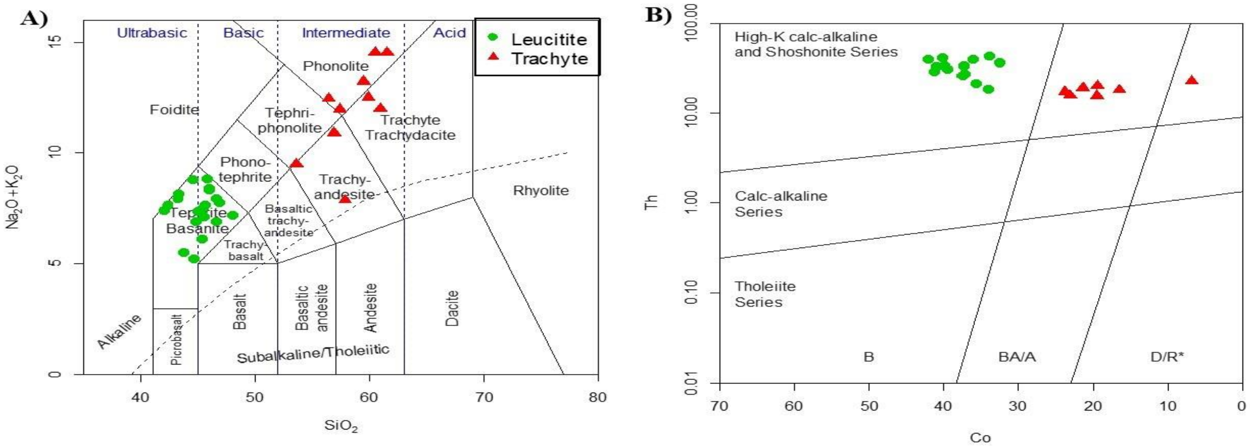

Figure 13: A) SiO_2 vs. Na_2O+K_2O plot showing the classification of volcanic rocks (Le Bas et al., 1986). B) Co-Th plot illustrating the calc-alkaline and high-potassium shoshonitic nature of volcanic rocks (Hastie et al., 2007).

Table 3 - Data on the main elements of the whole rock

Sample No	Aq077	Aq150	Aq267	Aq288	Aq312	Br431	A	A-1	A-3	PL-1-a	T-1-x	T-4-b-1	T-4-b-2
Type	Xenolith in leucitite	Xenolith in leucitite	Xenolith in leucitite	Xenolith in leucitite	Xenolith in leucitite	Xenolith in leucitite	Xenolith in trachyte	Xenolith in trachyte	Xenolith in trachyte	Xenolith in leucitite	Xenolith in trachyte	Xenolith in trachyte	Xenolith in trachyte
SiO_2	40.275	43.726	40.555	37.839	41	35.274	33.166	38.112	41.989	37.613	31.123	33.71	34.287
Al_2O_3	9.753	13.945	11.669	12.313	12.588	8.933	8.043	5.813	9.138	8.871	8.024	7.921	8.086
Fe_2O_3	11.307	10.815	13.94	12.138	11.915	12.873	19.388	9.945	11.367	12.732	11.27	15.041	14.466
CaO	13.145	10.724	13.411	13.12	13.583	20.23	17.324	23.634	13.76	14.398	22.806	18.637	18.291
MgO	7.37	4.036	4.97	10.116	6.328	7.863	9.503	13.35	9.306	9.6	7.348	12.98	13.542
Na_2O	1.971	1.634	1.299	1.28	2.263	1.251	0.451	0.317	0.6	0.733	0.37	0.315	0.297
K_2O	6.265	8.475	7.457	5.171	6.824	4.109	4.522	3.181	7.617	6.726	4.784	4.675	4.413
SO_3	0.082	<.1	<.1	<.1	<.1	0.093	<.1	<.1	<.1	0.1	<.1	<.1	<.1
P_2O_5	0.737	1.214	1.577	1.232	1.456	3.368	2.63	3.12	2.364	1.147	1.593	2.323	2.349
MnO	0.37	0.155	0.2	0.217	0.184	0.34	0.319	0.214	0.297	0.176	0.314	0.287	0.29
TiO_2	1.521	1.347	1.854	1.7	1.402	2.363	3.017	1.572	2.284	1.751	2.192	2.823	2.664
CuO		-	-	<.1	<.1		<.1	<.1	<.1	<.1	<.1	<.1	<.1
BaO	0.487	0.511	<.1	0.485	0.347	1.161	0.586	<.1	0.428	0.42	0.3384	0.297	0.3445
SrO	0.168	0.233	0.22	0.178	0.182	0.248	0.1	0.112	0.176	0.142	0.133	<.1	<.1
ZrO_2	<.1	<.1	<.1	0.07	<.1	<.1	<.1	-	<.1	0.075	<.1	-	-
Cl	<.1	<.1	0.231	<.1	<.1	0.105							
ZnO							<.1	<.1	<.1	<.1	<.1	<.1	<.1
L.O.I.*	6.34	2.98	2.43	3.94	1.76	1.59	0.75	0.43	0.43	5.32	9.49	0.71	0.71

Sample No	T-4-x-1	T-4-x-2	T-6-x	Ga025	Ga097	Ga217	Qb-3	Qb-4	Qb-7	Qb-9	Aq243	Ad-6	Aq110
Type	Xenolith in trachyte	Xenolith in trachyte	Xenolith in trachyte	Xenolith in leucitite	Xenolith in leucitite	Xenolith in leucitite	Xenolith in leucitite	Xenolith in leucitite	Xenolith in leucitite	Xenolith in leucitite	Trachyte	Trachyte	Trachyte
SiO_2	33.4	33.305	38.561	43.183	40.596	43.433	39.587	40.088	39.008	43.156	49.446	55.852	58.4719
Al_2O_3	8.729	8.109	7.017	14.135	16.554	12.203	14.392	13.363	12.61	13.001	16.819	15.281	16.468
Fe_2O_3	12.388	12.776	13.588	10.283	10.896	11.002	12.1	11.891	10.346	10.484	6.058	6.388	6.078
CaO	19.433	19.931	17.604	10.686	12.278	10.668	12.507	13.095	12.908	10.775	8.123	6.265	2.218
MgO	8.801	8.899	12.261	6.469	4.297	7.768	5.103	6.253	7.065	6.121	1.765	2.034	0.939
Na_2O	0.369	0.313	0.739	2.368	5.614	0.53	2.749	2.376	1.111	1.346	3.429	4.009	3.02
K_2O	5.604	5.415	3.904	7.529	2.15	9.376	6.984	6.602	7.069	8.455	5.341	6.708	9.987
SO_3	<.1	<.1	<.1	<.1	<.1	<.1	<.1	<.1	<.1	<.1	<.1	0.161	<.1
P_2O_5	1.858	1.779	2.284	1.203	1.415	1.627	1.684	1.571	1.436	1.148	0.324	0.691	0.229
MnO	0.35	0.344	0.255	0.226	0.332	0.219	0.356	0.386	0.367	0.327	0.182	0.132	<.1
TiO_2	2.254	2.379	2.377	1.068	1.28	1.866	1.374	1.494	1.238	1.2	0.756	0.799	0.917
CuO	<.1	<.1	<.1	<.1	-	<.1					-		-
BaO	0.3355	0.3372	0.392	0.354	0.529	0.426	0.39	0.442	0.332	0.281	0.304	<.1	<.1
SrO	0.135	0.127	<.1	0.171	0.239	0.233	0.21	0.228	0.139	0.146	0.18	0.142	0.15
ZrO_2	-	<.1	<.1	<.1	<.1	<.1	<.1	<.1	<.1	<.1	<.1	<.1	<.1
Cl					-	-	0.184	0.105	<.1	<.1	<.1	<.1	<.1
ZnO	<.1	<.1	<.1										
L.O.I.*	6.16	6.04	0.81	2.09	3.62	0.44	2.2	1.87	6.17	3.32	7.05	1.34	1.31

https://doi.org/10.5281/zenodo.15010171

Sam1ple No	Aq141	Aq145b	Aq145c	Aq435	T-6	Qb425a	Qb425b	Ad-8	Aq055	Aq060	Aq082	Aq084	Aq086
Type	**Trachyte**	**Trachyte**	**Trachyte**	**Trachyte**	**Trachyte**	**Trachyte**	**Trachyte**	**Leucitite**	**Leucitite**	**Leucitite**	**Leucitite**	**Leucitite**	**Leucitite**
SiO_2	57.079	55.0505	56.029	59.371	60.361	60.298	58.922	43.378	42.056	39.203	43.77	45.553	44.323
Al_2O_3	17.003	16.635	16.527	16.237	15.765	18.232	18	12.717	10.032	11.105	12.635	14.493	13.271
Fe_2O_3	6.703	6.397	6.122	5.108	5.323	2.603	2.693	10.389	10.861	10.995	11.454	9.961	10.682
CaO	6.742	5.059	4.655	3.335	3.424	1.988	3.126	11.231	15.804	12.05	10.308	11.023	10.53
MgO	2.236	0.973	1.247	1.345	1.364	0.259	0.216	6.077	9.453	6.329	5.433	3.814	5.446
Na_2O	4.513	3.004	3.108	3.843	4.791	5.067	3.845	3.258	2.617	0.791	4.446	3.646	4.479
K_2O	3.26	9.173	8.597	8.583	7.102	9.188	10.332	3.157	2.674	6.396	3.546	3.157	3.071
SO_3	<.1	<.1	<.1	<.1	<.1	<.1	<.1	<.1	<.1	<.1	<.1	<.1	<.1
P2O5	0.354	0.35	0.336	0.465	0.334	0.063	<.1	1.468	1.168	1.729	1.655	1.373	1.27
MnO	0.149	0.159	0.235	0.121	<.1	<.1	<.1	<.1	0.246	0.309	0.252	0.19	0.329
TiO_2	0.683	0.809	0.795	0.741	0.636	0.328	0.314	1.324	1.217	1.653	1.664	1.502	1.596
CuO	-	<.1		-	<.1	-			<.1		<.1	<.1	
BaO	0.159	0.345	0.286	<.1	0.1495	<.1	0.183	0.404	0.426	0.501	0.401	0.301	0.351
SrO	0.148	0.232	0.204	0.161	0.152	0.195	0.306	0.159	0.173	0.25	0.174	0.134	0.142
ZrO_2	<.1	<.1	<.1	0.08	<.1	0.155	<.1	<.1	<.1	<.1	<.1	<.1	<.1
Cl	<.1	-	<.1	-		0.158	-	-		-			<.1
ZnO					<.1								
L.O.I.*	0.76	1.59	1.61	0.38	0.35	1.23	1.83	6.21	3	8.49	4	4.6	4.28

Sam1ple No	Aq130	Aq134	Aq145a	Aq439a	L-2-b	PL-1-b	Ga034	Ga041	Ga091	Ga196	Ga309	Ga438	Qb-2	Qb
Type	**Leucitite**	**Leucitite**	**Leucitite**	**Leucitite**	**Leucitite**	**Leucitite**	**Leucitite**	**Leucitite**	**Leucitite**	**Leucitite**	**Leucitite**	**Leucitite**	**Leucitite**	**Leu**
SiO_2	43.748	41.812	41.134	42.924	40.435	39.505	43.101	43.281	44.187	42.703	44.295	42.867	42.846	44.
Al_2O_3	15.799	13.476	9.908	9.264	9.576	8.837	13.219	14.002	15.049	15.036	14.332	11.846	13.561	14.
Fe_2O_3	10.277	11.342	12.182	10.467	11.848	11.888	10.063	11.389	10.154	12.498	9.03	12.892	10.069	10.
CaO	12.088	11.294	12.97	15.321	14.126	13.826	13.187	12.34	12.299	12.483	11.946	11.792	12.405	11.
MgO	3.668	3.707	6.677	10.595	8.976	10.084	5.331	5.142	3.82	3.217	5.569	5.157	7.166	5.
Na_2O	4.434	3.163	0.57	3.717	0.996	0.835	3.973	3.459	4.414	3.652	3.237	1.581	3.22	1.
K_2O	2.908	3.735	7.175	1.317	6.298	6.153	2.749	3.633	3.576	2.934	5.297	6.876	2.564	5.
SO_3	<.1	<.1	<.1	0.09	<.1	0.1	<.1	<.1	<.1	<.1	<.1	<.1	<.1	<
P_2O_5	1.247	1.42	1.961	1.095	1.22	1.166	1.448	1.215	1.225	1.094	1.274	1.231	1.114	1.
MnO	0.299	0.37	0.229	0.217	0.315	0.193	0.197	0.23	0.174	0.233	0.182	0.228	0.312	0.
TiO_2	1.309	1.642	2.189	1.128	1.607	1.636	1.248	1.458	1.101	1.314	1.516	1.663	1.227	1.
CuO	-		<.1	0.154	<.1	<.1	<.1	<.1	<.1	-	<.1	<.1		
BaO	0.393	0.494	0.32	0.415	0.316	0.3407	0.508	0.406	0.435	0.468	0.362	0.635	0.326	0.
SrO	0.19	0.205	0.136	0.157	0.128	0.131	0.216	0.195	0.194	0.264	0.18	0.263	0.18	0.
ZrO_2	<.1	<.1	0.108	<.1	<.1	<.1	<.1	<.1	<.1	0.093	<.1	<.1	<.1	<
Cl	<.1	<.1	-	-						-	<.1	-	-	<
ZnO					<.1	<.1								
L.O.I.*	3.44	7.14	4.24	2.94	3.96	5.1	4.56	3.08	3.17	3.81	2.58	2.77	4.81	4.

https://doi.org/10.5281/zenodo.15010171

Table 4 - Data on minor elements of the whole rock

Sample No	**Aq077**	**Aq150**	**Aq267**	**Aq288**	**Aq312**	**Br431**	**A**	**A-1**	**A-3**	**PL-1-a**	**T-1-x**	**T-4-b-1**	**T-4-b-2**
Type	**Xenolith in leucitite**	**Xenolith in leucitite**	**Xenolith in leucitite**	**Xenolith in leucitite**	**Xenolith in leucitite**	**Xenolith in leucitite**	**Xenolith in trachyte**	**Xenolith in trachyte**	**Xenolith in trachyte**	**Xenolith in leucitite**	**Xenolith in trachyte**	**Xenolith in trachyte**	**Xenolith in trachyte**
Ag		1.0449	1.5747	1.306	1		<1	1	1	1.1584	1.5169	<1	<1
As		5.95379	7.97345	14.8615	4.50054		12.848	15.5618	9.59461	4.00659	8.73792	6.4819	4.88727
Ba		4200.94	2661.32	4108.9	4127.36		3265.17	2127.55	7079.19	3252.04	2871.02	3097.82	3119.6
Be		10.8184	12.9681	6.79353	8.70947		8.05654	4.10237	19.656	6.56484	5.57704	0.803086	0.94265
Cd		0.24232	0.236094	0.190885	0.391928		0.243801	0.286629	0.358551	0.424251	0.688595	0.242188	0.300274
Ce		171.755	195.68	148.28	186.019		218.814	104.937	279.983	119.078	196.895	105.702	102.787
Co		38.6646	41.4833	46.8988	42.341		65.234	40.3188	86.083	41.7317	38.987	52.068	48.7039
Cr		40.2357	30.7744	594.434	170.72		92.273	473.34	629.514	399.914	224.282	339.968	331.824
Cu		87.25293	148.4918	90.04195	127.8614		227.5974	29.11608	44.02362	108.2764	157.099	16.81882	16.21178
Dy		11.3232	13.5477	10.3373	11.3824		14.3411	7.93359	17.3627	8.36548	12.482	9.69753	9.67922
Er		6.93569	8.40491	6.51032	5.51568		7.44818	5.39341	9.01498	6.26952	6.71332	6.28563	5.37771
Eu		3.31347	4.29987	2.93192	3.56377		4.70002	2.62433	6.17392	2.43965	4.03066	2.84125	2.50715
Ga		18.6041	23.5339	17.0248	22.2082		19.5856	9.74447	31.1963	19.8653	15.7182	16.2362	15.5465
Gd		10.6203	13.2117	9.47158	11.145		15.8196	8.41557	18.6158	9.05669	11.1756	10.8843	10.8033
Ge		1.24144	3.87899	1	1.5731		4.3937	2.4887	2.76273	3.99171	4.43768	2.6728	2.51208
Hf		29.6951	22.9208	13.5986	12.4838		14.3019	4.59463	32.0105	11.0663	8.50549	21.6528	10.0328
Ho		2.04669	2.50596	1.75153	2.04306		3.1604	1.55186	3.9303	1.49656	2.40713	1.60819	1.6098
La		96.1325	106.943	84.4323	105.104		114.024	62.0449	149.887	65.611	108.486	52.8251	52.4139
Li		9.44262	9.29884	8.224	8.28026		15.5159	17.462	15.2554	8.28798	19.3607	1.66361	1.44136
Lu		0.3488	0.441325	0.346812	0.39724		0.534304	0.261186	0.601524	0.350546	0.325032	0.392143	0.381142
Mn		1407.34	1925.17	1405.31	1665.9		2071.64	1306.97	2263.38	1455.15	2222.19	1355.9	1351.9
Mo		0.712725	0.590396	0.860583	0.5		<0.5	0.819368	<0.5	<0.5	<0.5	<0.5	<0.5
Nb		60.82379	60.5957	46.90045	54.68338		34.09049	14.77033	95.76382	30.3386	29.6318	23.7699	20.45518
Nd		85.7875	105.814	72.5553	82.8054		134.904	66.9896	167.361	60.534	106.688	68.5449	67.6043
Ni		29.3455	23.621	90.492	41.3676		37.7445	80.1328	93.1475	70.4947	54.5731	59.7028	62.9187
P		6486.79	7123.84	6076.55	7542.17		>10000	>10000	>10000	5115.96	>10000	>10000	7780.4
Pb		30.5012	48.0149	31.4523	45.8075		19.8359	8.76968	19.1252	26.136	91.1412	9.34858	22.0292
Pr		18.6684	24.4185	16.9809	19.2902		29.1778	14.4756	35.3718	15.7535	21.4205	17.1634	17.2347
Rb		284.5	498.917	141.864	178.234		172.491	139.987	271.773	169.689	140.184	66.9972	62.2237
S		214.298	279.894	278.673	154.973		519.11	360.37	375.695	1085.58	540.172	347.824	350.808
Sc		34.3526	46.1418	40.9183	45.158		75.6706	88.1716	71.8401	48.2552	58.6346	81.7405	80.5898
Sm		15.9699	20.0183	13.3889	15.1227		24.7004	12.2831	31.8625	11.4908	18.9987	12.62	12.908
Sr		1250.96	1333.97	925.042	1159.73		484.326	622.853	1630.62	817.893	735.958	426.863	425.785
Ta		3.28158	6.0632	2.71129	3.41351		7.27456	3.20038	4.96822	5.04499	8.84655	2.18333	4.81672
Tb		1.63633	2.01399	1.75934	1.85957		2.22809	1.11598	2.78973	1.47103	1.84524	1.12875	1.33152
Te		0.634088	1.09525	0.703789	0.807806		1.53114	0.626334	1.3535	0.800875	0.652095	0.942959	0.977595
Th		24.0027	49.106	17.1078	24.1412		49.9407	20.1052	34.5643	40.9932	42.497	28.8223	31.6782
Tl		0.802913	1.1409	0.518017	1.49347		1.26298	1.74503	0.97016	1.39338	1.01506	0.967745	1.33373
Tm		0.300365	0.587917	0.21928	0.293438		0.7853	0.334449	0.516817	0.581542	0.733167	0.466916	0.500337
Ti		8677.47	8707.98	8651.04	8386.25		>10000	2193.43	>10000	5918.28	7940.98	>10000	4982.77
U		6.762867	8.293209	6.078269	7.307363		9.799498	4.699005	11.29335	6.455259	5.973915	7.028958	6.918019
V		242.303	322.853	212.986	274.943		351.666	128.602	348.575	218.077	244.414	274.054	237.029
Y		54.2972	59.4609	47.5037	53.121		58.3162	36.1057	74.2684	39.0696	54.1397	41.8043	42.9528
Yb		3.87576	4.69064	4.17497	4.38115		4.7276	3.15027	7.04868	3.54374	4.60985	3.75797	3.29235
Zn		54.7967	94.2652	116.867	44.6851		99.8855	59.6265	72.9087	114.149	157.741	39.2586	42.8061
Zr		1335.77	1287.3	759.757	1111.94		361.676	187.225	922.969	763.243	431.885	270.667	252.032

https://doi.org/10.5281/zenodo.15010171

Sample No	T-4-x-1	T-4-x-2	T-6-x	Ga025	Ga097	Ga217	Qb-3	Qb-4	Qb-7	Qb-9	Aq243	Ad-6	Aq110
Type	Xenolith in trachyte	Xenolith in trachyte	Xenolith in trachyte	Xenolith in leucitite	Xenolith in leucitite	Xenolith in leucitite	Xenolith in leucitite	Xenolith in leucitite	Xenolith in leucitite	Xenolith in leucitite	Trachyte	Trachyte	Trachyte
Ag	1.1413	1.1983	<1	1	1.3196	1					1		<1
As	6.03777	7.65174	3.9356	<2	10.0104	<2					10.8982		6.47775
Ba	2912.86	2793.54	2521.51	3160.92	4508.45	3459.1					3500.97		1862.39
Be	7.15251	6.41956	3.23389	7.91588	6.43487	10.7804					19.168		20.9613
Cd	0.36976	0.199798	0.1558	0.386308	0.377591	0.222624					0.312901		0.471695
Ce	159.372	159.366	192.075	134.187	162.315	124.512					166.863		167.037
Co	44.9744	45.5553	47.0231	36.6173	33.8404	35.9765					21.3762		16.5156
Cr	215.597	216.824	680.392	115.434	94.6787	194.781					50.0687		19.8814
Cu	174.6069	158.1451	28.76395	123.5886	158.9672	22.51446					58.58899		56.37755
Dy	10.9649	10.5988	11.2244	9.24238	9.48445	6.89934					7.8295		8.53434
Er	6.41601	5.86925	6.55006	5.62559	5.54254	3.24193					4.5843		4.83569
Eu	3.56338	3.78404	4.08313	2.56627	2.94605	2.62053					2.54321		2.80914
Ga	17.1788	12.8229	14.638	18.1605	18.4627	16.6948					18.933		20.4062
Gd	10.3725	10.2456	11.8289	9.13111	9.29139	8.05992					6.80207		7.33159
Ge	3.05612	3.402	3.22473	3.50899	1	1.95631					1.10276		0.975363
Hf	8.09286	10.5551	12.8051	20.4351	12.4742	6.33888					26.61		53.192
Ho	2.19281	2.00896	2.68627	1.58912	1.88415	1.58885					1.57044		1.55038
La	89.4693	85.9604	103.974	78.9656	104.511	66.8884					103.553		96.9065
Li	18.0254	16.7471	28.8611	8.79819	15.0024	4.52842					6.73022		21.9456
Lu	0.324262	0.313628	0.379088	0.341219	0.347017	0.272					0.221583		0.214126
Mn	1773.19	1743.37	1623.56	1521.01	1313.36	1201.7					1447.22		1091.05
Mo	<0.5	<0.5	0.717371	0.615971	<0.5	0.567058					0.958441		<0.5
Nb	28.04604	35.90957	20.20787	44.3621	43.60901	32.76376					71.5976		120.9124
Nd	91.7387	87.7216	112.525	66.3455	78.1883	71.5214					67.9239		67.461
Ni	64.5962	62.6412	82.1759	42.8932	34.4952	31.5048					7.77411		6.30266
P	>10000	>10000	7790.91	5836.43	5833.7	9307.21					2095.63		1468.62
Pb	37.3329	49.571	10.0122	35.4003	58.0216	10.4291					95.1163		83.7913
Pr	20.2303	17.4015	24.0502	17.499	20.923	15.1994					15.6295		15.2837
Rb	153.297	143.86	138.567	193.075	116.34	216.743					338.292		261.668
S	412.494	551.267	285.381	167.26	190.908	161.134					314.872		195.016
Sc	58.3327	59.6814	61.5513	32.5836	24.4709	41.647					12.5987		9.15025
Sm	16.7798	16.0806	20.3312	12.0306	13.5312	12.6638					11.7282		11.7489
Sr	725.453	698.229	432.6	1003.55	1335.82	1202.51					1059.61		951.574
Ta	6.50634	6.62697	3.74723	4.64664	2.42484	3.28354					1.46427		2.5016
Tb	1.3592	1.17229	1.2212	1.57678	1.46686	1.04888					1.23728		1.41368
Te	0.491344	0.569767	0.779701	0.511999	0.751391	0.456277					0.309473		0.277694
Th	34.147	36.2055	34.9107	39.5982	16.7865	25.9296					19.1452		18.158
Tl	0.899877	1.44287	0.674841	0.5	0.986214	1.03126					1.31208		0.867097
Tm	0.575444	0.633042	0.544321	0.547797	0.200903	0.319361					0.201692		0.152865
Ti	7622.39	>10000	4408.74	6738.98	7156.54	7754.51					5588.98		5766.15
U	5.666175	5.88227	6.560704	6.215218	6.815675	5.234222					4.7242		4.486406
V	231.039	241.44	213.623	223.575	241.077	164.069					212.584		177.583
Y	46.4748	45.2291	47.8298	41.218	38.9193	31.5108					36.7361		37.5724
Yb	3.79134	4.39859	3.94346	4.01902	3.04052	2.83309					3.51099		3.63744
Zn	97.044	114.696	79.1035	68.4034	227.944	66.2678					116.592		208.413
Zr	353.887	359.766	280.204	837.617	735.471	456.432					1546.52		2669.95

Sam1ple No	Aq141	Aq145b	Aq145c	Aq435	T-6	Qb425a	Qb425b	Ad-8	Aq055	Aq060	Aq082	Aq084	Aq086
Type	Trachyte	Trachyte	Trachyte	Trachyte	Trachyte	Trachyte	Trachyte	Leucitite	Leucitite	Leucitite	Leucitite	Leucitite	Leucitite
Ag	<1	<1		<1	<1	1.1989			1.2784		1.5096	1.1704	
As	3.83935	18.0445		6.72262	12.1526	14.0286			7.57457		6.4647	5.78268	
Ba	2358.96	3105.44		2530.57	2332.47	1412.16			3147.6		4046.43	3011.17	

Be	2.75214	17.8343		12.441	9.65796	28.4669			7.15578		12.859	11.5911	
Cd	0.389248	0.386905		0.129659	0.144757	0.355485			0.21564		0.389158	0.305345	
Ce	93.6662	156.6		98.2323	104.401	124.448			109.89		145.715	143.948	
Co	23.7887	19.4298		23.0829	19.4849	6.80775			39.4958		42.0713	32.5177	
Cr	50.67	20.2575		54.4594	64.1277	3.61325			665.103		183.313	236.261	
Cu	53.06269	75.94138		83.90984	52.75368	13.1544			91.18659		136.0374	124.4006	
Dy	4.55151	7.59859		4.90312	5.25003	4.31084			8.36219		9.35921	9.36892	
Er	4.01628	5.20298		3.0342	3.05873	3.80538			5.43919		5.76695	5.99294	
Eu	1.2998	2.29681		2.04018	1.88881	1.33348			2.22074		3.2475	2.97757	
Ga	18.0357	16.1513		16.9954	19.3164	20.8061			12.37		18.376	18.1138	
Gd	5.08873	6.33291		5.63327	5.34359	3.33977			8.10981		10.6542	8.66703	
Ge	1.58204	1.30073		1.14319	1.25491	1			2.45549		3.03926	3.49749	
Hf	10.3079	24.8932		21.0926	21.2248	50.9611			11.2394		16.0661	18.7171	
Ho	0.833792	1.37195		1.07518	1.11768	0.763684			1.38657		1.9349	1.56189	
La	60.5869	81.2773		48.6016	54.6525	63.0708			63.7316		90.7374	79.267	
Li	9.14999	12.6515		12.6586	13.4072	14.7842			8.45852		9.07165	6.70969	
Lu	0.21194	0.188988		0.193481	0.210679	0.117703			0.286483		0.349296	0.286446	
Mn	1037.99	1084.01		904.258	817.256	871.71			1234.41		1507.79	1316.35	
Mo	<0.5	<0.5		0.519353	1.05887	<0.5			1.28246		<0.5	<0.5	
Nb	22.05926	61.16768		47.67828	43.54529	81.09118			33.53683		56.11661	55.49902	
Nd	36.659	60.9265		47.6875	48.609	31.3067			58.7679		84.9212	69.2871	
Ni	16.6294	5.82502		28.3886	26.1886	<0.5			105.672		39.8054	24.3332	
P	1619.55	1724.87		3762.88	2604.45	380.182			4981.42		7958.51	6837.46	
Pb	43.7356	49.0091		49.5938	35.0018	56.9646			23.7752		49.8938	36.4223	
Pr	9.55683	13.467		10.5843	12.0033	7.46815			15.4232		20.5718	16.3259	
Rb	44.6185	199.51		190.499	200.85	177.213			98.3172		180.778	282.468	
S	138.799	217.974		202.923	241.317	193.692			293.787		530.867	253.94	
Sc	18.4	11.6622		16.2744	14.7312	1.79232			42.3555		34.499	35.7154	
Sm	5.86513	10.4961		8.82183	9.03462	5.61127			10.8758		15.9113	12.8544	
Sr	857.617	1278.77		1136.7	1085.01	978.583			868.87		1117.01	788.461	
Ta	1.50885	1.81117		1.63199	1.86524	2.34176			4.60572		6.15783	4.69173	
Tb	0.951242	1.18694		1.23692	1.0958	0.950039			1.49106		1.77897	1.52701	
Te	0.550906	0.465721		0.604323	0.154651	<0.02			0.509665		0.939018	0.809618	
Th	17.3916	20.2256		15.81	15.6814	22.8985			31.0721		40.192	36.5429	
Tl	0.77119	0.466103		0.580823	1.11832	1.0101			1.05847		0.5	0.591433	
Tm	0.228608	0.185865		0.173786	0.177753	0.189062			0.400917		0.5756	0.551845	
Ti	4652.94	5012.58		5372.92	5068.86	2587.68			5795.14		8761	8381.9	
U	3.815713	4.391765		4.381027	4.236692	2.426815			5.315405		6.562031	5.307809	
V	137.479	148.833		156.269	140.296	77.7233			183.426		363.468	278.355	
Y	23.9935	37.4992		23.9435	25.0528	25.1611			37.3395		43.3617	42.3809	
Yb	2.73533	3.69371		2.71386	2.8348	3.04105			3.60431		3.88996	3.93612	
Zn	60.1795	57.0701		43.6792	32.9313	49.9971			55.2473		84.9638	71.1154	
Zr	464.307	1574.59		1082.56	1011.48	2579.67			697.106		1100.53	998.699	

Sam1ple No	Aq130	Aq134	Aq145a	Aq439a	L-2-b	PL-1-b	Ga034	Ga041	Ga091	Ga196	Ga309	Ga438	Qb-2	Qb422
Type	Leucitite	Leucitite	Leucitite	Leucitite	Leucitite	Leucitite	Leucitite	Leucitite	Leucitite	Leucitite	Leucitite	Leucitite	Leucitite	Leucitite
Ag	1.029		1	1.0674	1	1.0403	1.3705	1	1	1	<1	1		
As	9.06637		12.6692	18.5025	7.04635	10.7186	9.01453	<2	10.5383	11.3475	19.6699	11.3945		
Ba	2781.47		1903.46	2795.53	3082	2984.86	4329.39	3028.11	3744.23	3892.8	3188.59	3110.76		
Be	5.76725		10.9132	6.03958	5.43157	6.30832	8.80135	5.59741	5.70118	5.54015	7.14124	14.029		
Cd	0.195851		0.247187	0.281066	0.423155	0.142971	0.323713	0.466327	0.184409	0.224626	0.394206	0.600266		
Ce	137.568		109.551	112.364	113.629	99.4785	153.119	124.677	151.706	185.591	156.172	173.13		
Co	33.9423		40.9957	39.8627	41.3139	40.1996	37.4831	36.0882	37.3665	34.0782	35.6966	37.2509		
Cr	19.6581		165.548	783.797	377.75	373.14	202.336	110.311	64.828	10.5703	177.289	137.409		

Cu	99.65491		94.83264	77.32402	112.3886	106.7786	119.6653	98.0252	128.3699	93.96912	106.9392	98.45158		
Dy	7.99985		9.27457	7.24412	8.20902	7.89386	9.11328	8.8391	9.29364	9.80662	9.31273	9.32364		
Er	4.78011		5.66366	4.96016	5.32395	4.94096	5.72997	5.15495	6.05683	6.24726	5.29176	5.15699		
Eu	2.63462		2.37006	2.15318	2.52465	2.17978	2.54736	2.32354	2.86376	3.13021	2.89585	3.03558		
Ga	19.5063		16.1986	13.1884	17.4816	17.795	17.096	22.073	18.9011	20.7631	20.2885	18.7568		
Gd	8.5181		8.33992	7.88279	9.059	8.98646	9.31859	8.95261	9.65885	9.707	9.4333	9.02931		
Ge	3.95989		2.58632	2.90146	2.46127	4.16932	2.27411	3.36836	2.59534	1.0843	1.9743	2.30678		
Hf	14.4117		19.2666	12.519	16.9236	9.78873	12.0791	13.2029	12.7802	14.2701	12.9718	31.0948		
Ho	1.53642		1.33141	1.2822	1.49533	1.42782	1.60354	1.44789	1.75001	1.97492	1.80469	2.02678		
La	80.2222		54.7398	60.2938	66.1477	61.3718	85.5268	64.4633	87.6159	112.435	88.5912	87.599		
Li	8.49437		7.54074	7.80532	8.99667	8.45968	7.47878	8.48043	7.58159	8.84942	6.93438	9.56686		
Lu	0.322106		0.314231	0.294997	0.345994	0.335295	0.322604	0.355004	0.342885	0.329217	0.336578	0.298407		
Mn	1401.22		1264.44	1228.09	1426.37	1343.24	1448.93	1548.96	1520.47	1611.51	1449.15	1282.27		
Mo	0.653528		<0.5	<0.5	<0.5	<0.5	<0.5	0.810089	<0.5	1.14979	1.26862	1.35875		
Nb	45.91079		42.58036	23.98367	40.16753	32.13102	47.98559	46.07516	40.06268	33.49006	42.94024	65.64746		
Nd	62.8316		54.0157	55.307	62.943	60.0777	69.6628	58.3122	71.8443	81.719	76.4716	88.9143		
Ni	10.0839		29.5159	104.72	65.7018	68.4169	34.3104	30.212	17.5914	13.9884	30.2498	37.1473		
P	4686.74		8829.37	4473.9	6356.08	5594.44	6199.2	5728.65	4858.06	5165.23	5405.15	6912.88		
Pb	30.0494		30.0065	44.6613	22.5763	23.5983	38.3686	31.0662	42.3217	48.2603	24.4746	43.1769		
Pr	15.8668		14.0279	13.7505	17.0052	15.4683	17.0357	14.619	18.1039	19.8837	18.0134	18.8828		
Rb	33.6168		283.56	51.8722	153.35	171.209	133.574	18.5907	59.2089	98.7612	67.8525	176.748		
S	280.413		244.863	574.937	366.676	938.005	242.508	236.642	322.855	94.6507	273.685	301.216		
Sc	28.3986		38.2141	47.068	46.0872	46.3029	39.1657	31.2281	34.0755	22.1218	40.5082	31.744		
Sm	11.4532		10.9068	10.6175	11.7102	10.9882	12.7563	10.8638	13.2816	14.0968	14.1281	15.8132		
Sr	1026.25		668.235	810.463	671.689	785.883	1239.76	1031.29	1097.81	1316.02	924.677	1100.02		
Ta	5.33261		4.4624	6.12283	4.56014	5.71365	3.92343	6.2144	5.3547	2.12843	2.04922	3.70209		
Tb	1.60766		1.52172	1.60178	1.55375	1.40354	1.62694	1.60932	1.58914	1.61098	1.70625	1.51098		
Te	0.64936		0.749369	0.474063	0.737906	0.619836	0.773515	0.606173	0.684173	0.854042	0.75133	0.800809		
Th	42.994		33.0003	33.8318	29.1373	41.2617	26.3771	39.7419	33.7408	18.7452	21.6125	27.317		
Tl	0.87145		0.975225	1.19209	0.831169	0.659635	1.77803	0.853291	1.01289	0.98424	1.02655	1.03176		
Tm	0.518212		0.448827	0.453646	0.407127	0.601161	0.353359	0.540438	0.438923	0.200656	0.266318	0.307937		
Ti	8277.05		>10000	5437.08	8238.37	6603.31	7504.99	>10000	7321.76	6410.48	8482.93	8271.66		
U	5.664256		5.473001	4.95583	5.969236	6.315629	6.505346	6.620307	6.529634	6.773211	6.611501	6.04461		
V	299.506		136.312	177.944	221.099	211.252	244.211	259.536	258.134	283.564	247.856	217.319		
Y	38.6556		44.7451	35.1562	35.5286	36.3587	42.0457	39.3634	44.1916	45.9074	45.1754	41.8643		
Yb	3.80804		4.06005	3.23653	3.57181	3.40238	3.91366	4.22378	4.21087	4.13946	4.1382	3.56824		
Zn	78.389		56.8497	53.312	57.8586	77.6837	54.2285	65.3589	58.618	27.9275	48.2606	57.1301		
Zr	673.284		1247.12	635.309	689.306	712.747	871.163	785.615	785.563	786.985	908.043	1416.55		

In the spider diagram normalized to the primitive mantle (McDonough and Sun, 1995) for the host rock samples (Figures 14-A and 14-C), a positive anomaly indicative of incompatible large-ion lithophile elements (LILE) is observed for elements such as Rb, Ba, Th, La, and U. Depletions are evident for elements such as Lu, Yb, and Y. Negative anomalies of Ti, Zr, P, and Nb, along with a positive anomaly for Pb, are also present, while enrichment of LILE, including Rb, Ba, K, and Th, is notable in most samples. The negative anomaly of P, alongside negative anomalies of La and Ce, suggests lower amounts of apatite in the samples or the absence of these elements in the melt source. In the spider diagram normalized to Chondrite REE (Boynton, 1984), a downward trend is apparent for both trachyte and leucitite samples (Figures 14-B and 14-D).

https://doi.org/10.5281/zenodo.15010171

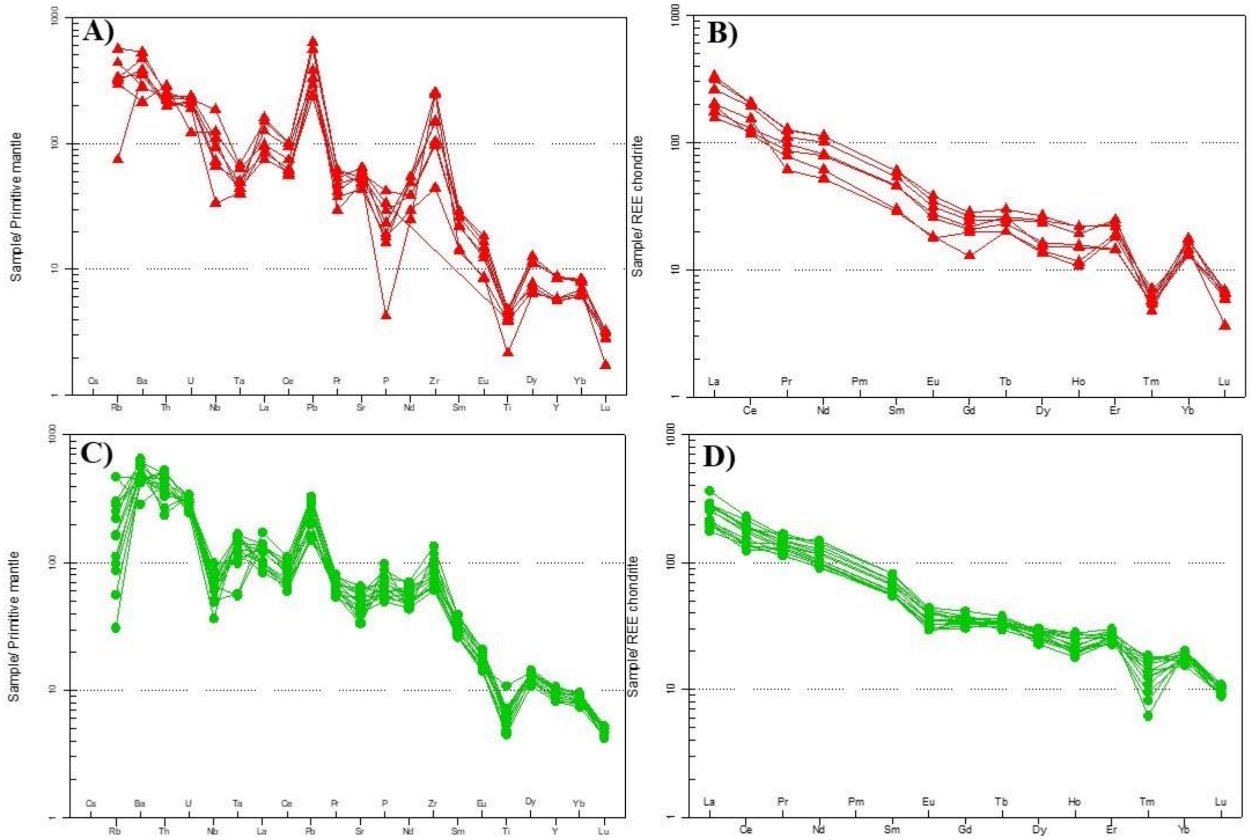

Figure 14: A) Spider diagram normalized to the early mantle (McDonough and Sun, 1995) for trachyte samples. B) Spider diagram normalized to the REE Chondrite (Boynton, 1984) for trachyte samples. C) Spider diagram normalized to the early mantle (McDonough and Sun, 1995) for leucite samples. D) Spider diagram normalized to the REE Chondrite (Boynton, 1984) for leucite samples.

Determination of tectonic environment

In the triangular diagram of TiO_2-K_2O-P_2O_5 (Pearce et al., 1975), oceanic basalts (MORB and basalts of oceanic islands) are positioned near the TiO_2 apex, while non-oceanic basalts are located below the boundary line. According to this diagram, the samples of leucitite host rock classify as continental basalts (Figure 15-A). To determine the tectonic environment, the Nb/16-Hf/3-Th triangular diagram (Wood, 1980) is used, where the leucitite host rock samples fall within the CAB range (calc-alkaline basalts) (Figure 15-B). Similarly, in the Ta/Yb-Th/Yb diagram (Pearce, 1982), the leucite host rock samples are situated in the basaltic volcanic arc range (Figure 15-C). Finally, in the Ta-Th diagram (Schandl and Gorton, 2002), all rock samples from leucite and trachyte hosts are positioned within the active continental margin (ACM) field (Figure 15-D).

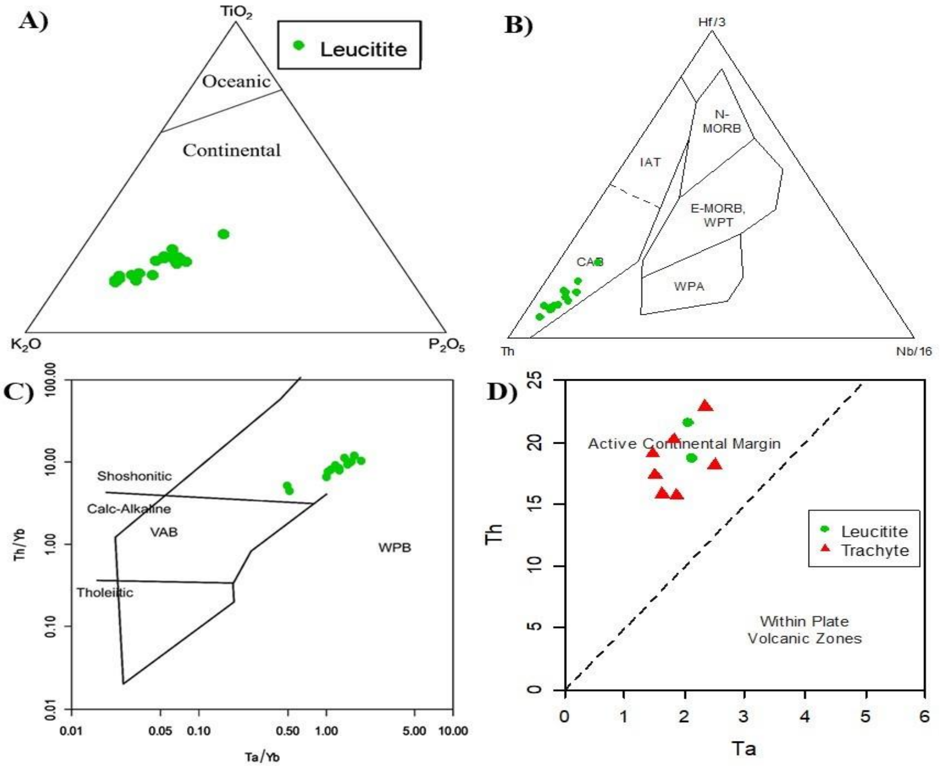

Figure 15: A) TiO_2-K_2O-P_2O_5 triangular diagram (Pearce et al., 1975). B) Nb/16-Hf/3-Th triangular diagram (Wood, 1980). C) Ta/Yb-Th/Yb diagram (Pearce, 1982) used for determining the tectonic environment. D) Ta-Th diagram (Schandl and Gorton, 2002).

Discussion

Heteromorphism refers to the crystallization of a single magma under varying physical conditions, leading to the formation of different rock types while maintaining the same chemical composition. An important indicator for examining changes in the chemical composition of pyroxenes is the magnesium number, defined as (Mg#=Mg/(Mg+Fe^{2+}). If the Mg# of clinopyroxene is greater than 0.7, the mineral is derived from the crystallization of a primary magma. In contrast, clinopyroxenes with Mg# less than 0.7 and rich in iron are formed from subtracted magmas (Deer et al., 1987).

- The average Mg# of clinopyroxene in pyroxenite xenoliths is 88.75, with the following ranges:
    - Clinopyroxene in trachyte host rock xenoliths: 84.18 to 95.59.
    - Clinopyroxene in leucitite host rock xenoliths: 81.84 to 96.87.
- The average Mg# in host rocks is:
    - Trachyte host rock: 91.91 (range: 91.82 to 92.12).
    - Leucitite host rock: 90.93 (range: 80.82 to 95.83).

The average Mg# of biotite minerals in pyroxenite xenoliths is 73.83, with ranges:

- Biotite in trachytic host rock xenoliths: 65.32 to 85.91.
- Biotite in leucitite host rock xenoliths: 71.60 to 76.57.

https://doi.org/10.5281/zenodo.15010171

For the host rocks:

- Trachyte host rock: 87.55 (range: 53.28 to 88.21).
- Leucitite host rock: 76.63 (range: 76.51 to 76.75).

The calculated Mg# suggests that these xenoliths represent the cumulus phases of the magma that produced the host volcanic rocks. Considering heteromorphism, which involves varying physical conditions (e.g., oxygen fugacity, depth) and consistent chemical composition (e.g., Mg#), and the presence of abundant biotite in pyroxenite xenoliths, it is inferred that the primary magma was rich in water and potassium. This facilitated the crystallization of biotite in magma reservoirs since the stability of micas and amphiboles depends on water availability.

Magma Composition and Origin

- **Water content**: High water concentration (>4–5% by weight) promotes amphibole crystallization, while relatively low water stabilizes biotite (Merzbacher & Eggler, 1984).
- **Elemental anomalies**:
    - Positive anomalies for Rb, Ba, Th, La, and U.
    - Depletion of Lu, Yb, and Y.
    - Negative anomalies for Ti, Nb, and Ta indicate subduction-related processes and possible crustal contamination (Gertisser & Keller, 2000; Rudnick & Gao, 2003).
- **Trace element enrichment**:
    - LILE (Rb, Ba, K) and LREE (La, Ce) suggest a metasomatized mantle source or crustal contamination.
    - Negative Ti, Nb, and Ta anomalies reflect subduction-related active continental margins.

The positive anomalies of K, Ba, and Rb are attributed to mica minerals (phlogopite and biotite) in the host rocks. The positive Pb anomaly indicates the involvement of sedimentary material in the magma source. Furthermore, the strong similarity in rare earth element (REE) distribution patterns between the two major rock groups (Figure 14) supports the hypothesis of a common parental magma and the process of heteromorphism (Ghadiri et al., 2020)

Pyroxenite Xenoliths

Pyroxenite xenoliths, primarily composed of pyroxene and biotite, exhibit:

- LREE enrichment relative to HREE in chondrite-normalized REE diagrams (Boynton, 1984).
- Positive anomalies for K, Pb, Rb, Ba, and U.
- Depletion in Ta and Nb due to biotite and clinopyroxene abundance.

The convex REE pattern (upward curvature) and low incompatible element concentrations suggest fractional differentiation of pyroxene from the melt (McDonough & Frey, 1989). The cumulus textures support mineral separation during crystallization.

https://doi.org/10.5281/zenodo.15010171

Fluids rich in K, Pb, Rb, Ba, and U likely facilitated the crystallization of biotite in the interstitial spaces of clinopyroxenes, enriching these elements.

In summary, pyroxenite xenoliths likely originated from metasomatized mantle material, followed by fractional crystallization and emplacement within host volcanic rocks. Figure 16 illustrates the REE enrichment and patterns for these samples.

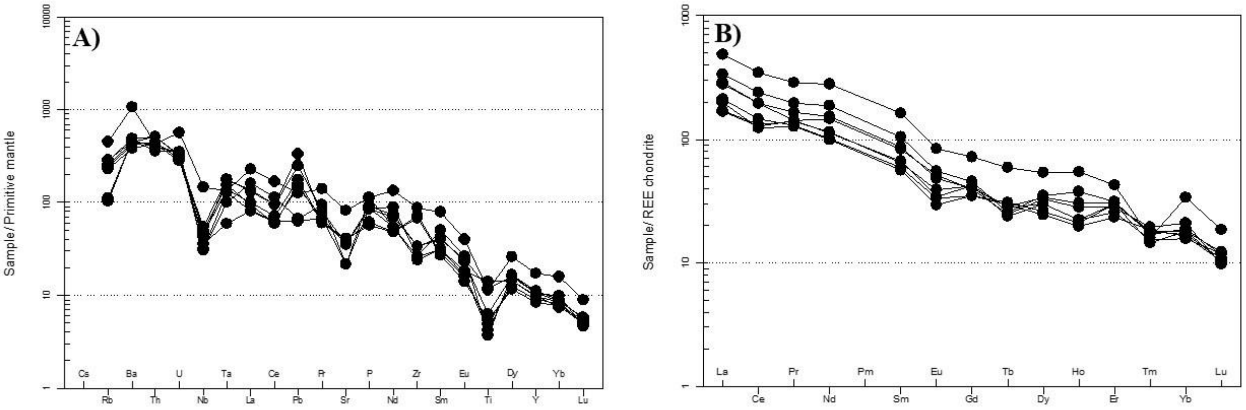

Figure 16: A**)** Spider diagram normalized to the early mantle (McDonough and Sun, 1995), illustrating elemental patterns in pyroxenite xenoliths and host volcanic rocks. B**)** REE chondrite-normalized spider diagram (Boynton, 1984), showing enrichment in light rare earth elements (LREE) relative to heavy rare earth elements (HREE), characteristic of pyroxenite xenoliths compared to their host volcanic rocks.

Petrogenesis of xenoliths and host rocks of the studied area

Ba/Ta and Ba/Nb ratios can be used to identify the origin of basaltic magmas (Fitton et al., 1991). High values of Ba/Ta > 450 and Ba/Nb > 28 are characteristic of magmatism related to subduction (Fitton et al., 1991). The Ba/Nb and Ba/Ta ratios in trachyte samples are 38.17 and 1285.94, in leucitite samples 74.3 and 699.47, and in xenolith samples 87.63 and 758.26. These values indicate the influence of subduction components in the magma that produced the rocks in the region. Considering the continental crust thickness in the studied area (42–43 km; Dehghani and Makris, 1984), there is a possibility of contamination of the magma by crustal materials. The ratio of (Ce/Pb)N in trachytic, leucitite , and xenolith rocks is 11.33, 6.37, and 0.19, respectively. This ratio is 47 in oceanic ridge basalts and 27 in arc basalts (Hoffman et al., 1986). The low Ce/Pb ratio in the host volcanic rocks indicates the presence of some crustal materials in the magma source (Yang et al., 2005). The amounts of Ni and Cr are 400 ppm and 600 ppm, respectively. In trachyte, leucitite, and xenolith rocks, the amounts of these elements are 15.2, 37.6, and 43.69 ppm for Ni, and 250.52, 56.57, and 284.99 ppm for Cr, respectively. The Rb/Y-Nb/Rb diagram can be used to identify enrichment by fluids in the subduction zone, crustal contamination, or enrichment in an intraplate setting (Temel et al., 1998). Vertical trends in this diagram appear as a result of subduction zone enrichment or crustal contamination, with an increase in the Rb/Y ratio. However, in intraplate enrichment, a positive trend is observed between Rb and Nb, and the Nb/Y ratio is equal to 1 (Temel et al., 1998). In this diagram, all samples exhibit a vertical trend (Figure 17-A), indicating enrichment by subduction zone fluids or crustal contamination. In the triangular diagram of 50Nb-3Zr-Ce/P2O5 (Müller et al., 1992), most of the samples fall within the post-collision range (Figure 17-B).

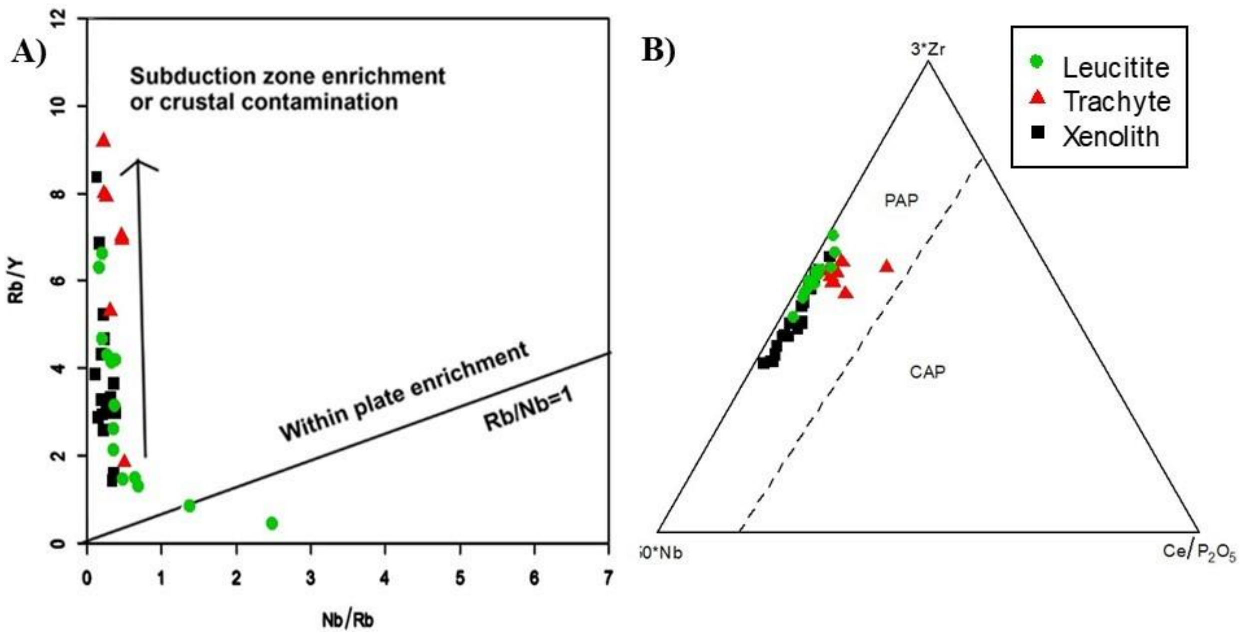

Figure 17: A) Rb/Y-Nb/Rb diagram (Temel et al., 1998), illustrating trends related to subduction zone enrichment or crustal contamination. B) Triangular diagram (Muller et al., 1992), showing the post-collision tectonic setting of the samples.

La/Sm vs. Sm/Yb and Sm vs. Sm/Yb diagrams have been used to identify the characteristics of the source of leucitite-hosting volcanic rocks (Figure 18-A and B). Data for the depleted mantle (DMM) are derived from McKenzie and O'Nions (1991), while data for the primitive mantle (PM) are from Sun and McDonough (1989). The La/Sm vs. Sm/Yb diagram suggests melting between garnet and spinel lherzolite sources (Figure 18-A). When spinel lherzolite begins to partially melt, both the mantle source and the resulting magma will exhibit consistent Sm/Yb ratios, while the La/Sm ratio will decrease as the degree of melting increases. Additionally, melting of the spinel lherzolite source produces a horizontal trend positioned within or near the mantle lines and the array determined by the combination of PM and DMM. In comparison, partial melting of a garnet-lherzolite source generates residual garnet with a high Sm/Yb ratio relative to the mantle source. As a result, the melting process of garnet lherzolite trends toward higher Sm/Yb values, diverging from the mantle array. In the Sm vs. Sm/Yb and La/Sm vs. Sm/Yb diagrams (Aldanmaz et al., 2000), the samples of leucitite-hosting volcanic rocks are located between the curves of garnet lherzolite and spinel garnet-lherzolite, indicating that garnet remained in the source of these samples. The scatter of the samples between the curves of garnet lherzolite and spinel garnet-lherzolite, and their distance from the DMM and PM fields, reflects the retention of garnet in their source. The scattered distribution of the samples also suggests varying degrees of melting and enrichment of their source. Among other elemental ratios useful for determining melting characteristics, the LREE/HREE versus HREE ratio is represented in the La/Yb versus Yb diagram (Figure 18-C) (Baker et al., 1997). These diagrams effectively distinguish melts derived from spinel and garnet fields (Thirlwall et al., 1994; Baker et al., 1997). The La/Yb ratio shows limited variation in spinel facies melts compared to their mantle source. In contrast, melts associated with garnet facies exhibit significant variations in Yb concentrations (Baker et al., 1997). A plausible model for the REE pattern of the rocks in the region suggests a mixture of a small proportion of spinel facies and a significant contribution from garnet facies (Figure 18-C).

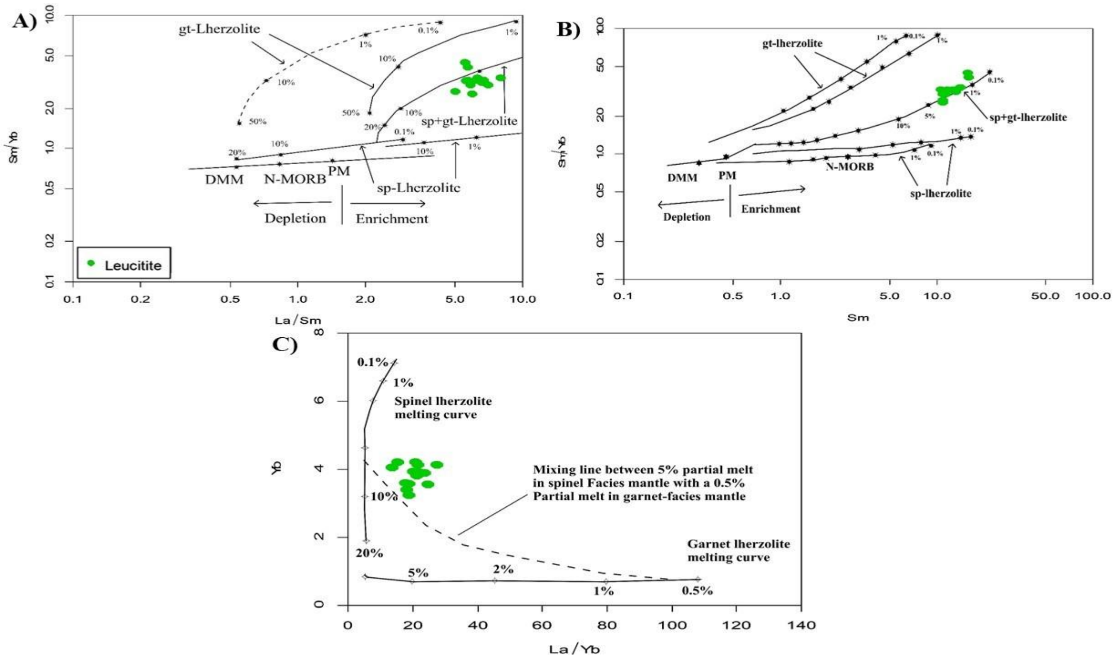

Figure 18: A) La/Sm vs. Sm/Yb diagram (Aldanmaz et al., 2000), B) Sm vs. Sm/Yb plot (Aldanmaz et al., 2000), C) Yb vs. La/Yb plot (Baker et al., 1997).

The magmatism of the Islamic Peninsula exhibits characteristics of shoshonitic and ultrapotassic magmas. The high concentrations of K_2O and MgO, along with relatively elevated levels of compatible minor elements in these rocks, suggest that their magma originates from the mantle. To account for the high K_2O content, the presence of a potassium-rich hydrous mineral in the mantle source is essential (Prelević et al., 2008; Lustrino et al., 2011). This is because the partial melting of a standard peridotite crust, even at very low degrees of partial melting, cannot produce ultrapotassic magma (Foley, 1992; Novella and Frost, 2014). In the La/Yb-Dy/Yb diagram (Prelević et al., 2012), most samples fall within or near the garnet mantle range, although some contribution from spinel in the mantle source is also plausible (Figure 19-A). This indicates a genetic connection between the xenoliths and leucitite host rocks. The La-La/Yb diagram (Vigouroux et al., 2008) reveals that the samples align along a trend emphasizing the presence of garnet and phlogopite minerals in the residual mantle source responsible for the magmatism of the Islamic Island (Figure 19-B). The degree of partial melting of the mantle peridotite required to produce the Islamic Island magmatism is estimated to be approximately 5–10%. Average TiO_2 values (0.93), a Zr/Hf ratio of 30, and variable Cs concentrations suggest that the region's rocks experienced carbonate metasomatism due to fluids released from the subducting oceanic plate (Salters et al., 2002; Zeng et al., 2010). Additionally, in the TiO_2-Na_2O+K_2O diagram (Zeng et al., 2010), all samples are consistent with the carbonate metasomatism of peridotite rocks (Figure 19-C).

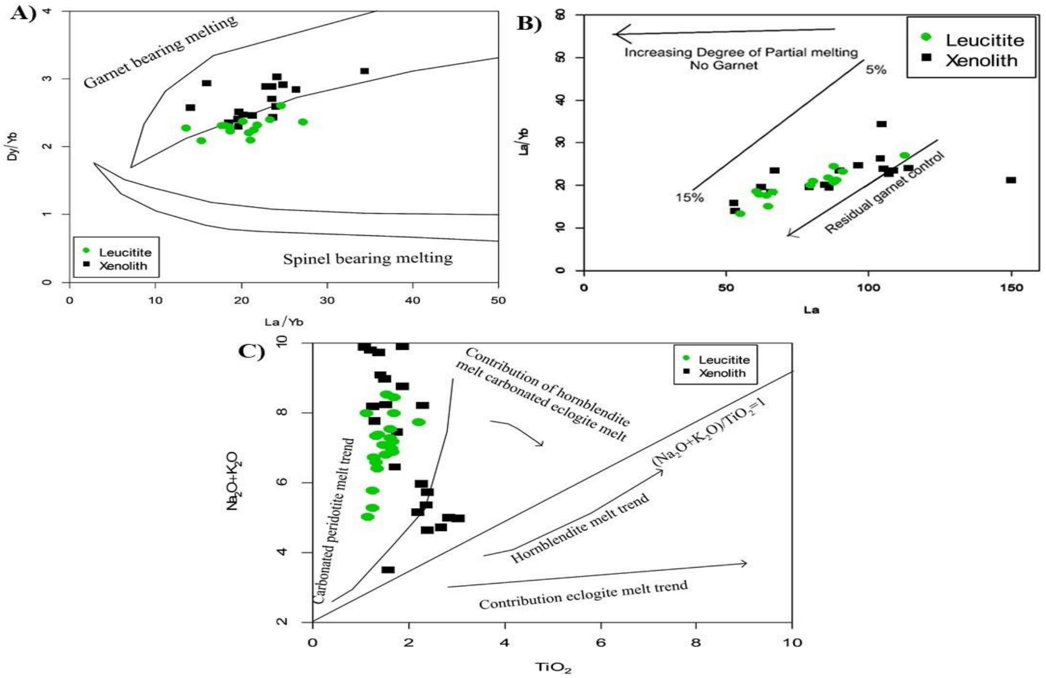

Figure 19: A) La/Yb-Dy/Yb diagram illustrating the mantle source characteristics, with data plotted in relation to the garnet and spinel mantle fields (Prelević et al., 2012). B) La-La/Yb diagram showing the trend indicative of garnet and phlogopite presence in the mantle residue responsible for magmatism in the Islamic Island region (Vigouroux et al., 2008). C) TiO_2-Na_2O+K_2O diagram highlighting the evidence of carbonate metasomatism in peridotite rocks (Zeng et al., 2010).

According to these explanations, the mantle composition responsible for Saray magmatism is likely micadar clinopyroxenite garnet. Such a heterogeneous assemblage could have formed within the lithospheric mantle. In the early stages of subduction, subducted sediments may have melted to produce silica-rich magma, which then interacted with the surrounding lithospheric mantle (Frost, 2006). As discussed in the geochemical and petrogenetic analyses, the source of the host volcanic rocks and most of the studied xenoliths exhibit elevated levels of LILE (large ion lithophile elements) and LREE (light rare earth elements), suggesting their origin from an enriched part of the mantle. Various source diagrams indicate that the formation environment of these rocks is associated with volcanic arcs. The subduction of the Neo-Tethys oceanic plate beneath the continental crust of Iran caused metasomatization of the overlying lithospheric mantle. This enrichment occurred through fluid release and melting of the subducted sediments or through acidic melts derived from the subducted plate. During continued subduction, steepening of the plate likely led to its fragmentation, forming a window or gap between the subducted fragments. Prolonged subduction processes caused significant contamination of the magmatic source. In the northern part of the Urmia-Dokhtar magmatic zone, magmatism ceased following the primary convergence period. This cessation is likely related to rollback processes and the eventual breaking off of the subducted plate (Ghasemi and Talbot, 2006; Jahangiri, 2007). Given the time elapsed between the closure of the Neo-Tethys and the eruption of the magmas forming the region's volcanic rocks, fault systems likely played a critical role in magma formation and ascent. Fault systems with ENE-WSW trends (left-lateral movement) and SSE-NNW trends (right-lateral movement) created a transtensional regime that facilitated magma ascent. As the magma ascended, it transported earlier cumulus phases to the surface. According to Moin-Vaziri (2001), the studied xenoliths are likely fragments of metasomatized mantle brought to the surface by the ascending magma. Given their formation depths of approximately 20 to 35 km, these xenoliths cannot represent primary mantle material.

conclusion

The Islamic Peninsula (Saray volcano) is situated in the northern section of the Urmia-Dokhtar magmatic belt, within the high Iranian-Turkish plateau. This volcano lies to the east of Lake Urmia and west of the Sahand volcano, consisting of alternating layers of lava and pyroclastics. The xenoliths found within the trachytic and leucitite host rocks vary in shape, with most being rounded and some polygonal. These xenoliths are predominantly black with a somewhat shiny appearance. The trachyte host rock primarily contains sanidine, biotite, and opaque minerals, while the leucitite host rock is dominated by leucite and pyroxene minerals. These minerals often form fine-grained textures featuring chimera-like mixtures of leucite, pyroxene, olivine, and opaque minerals. Most biotite in the leucitite host rock exhibits kink banding. Pyroxenite xenoliths within the trachyte and leucitite host rocks are composed mainly of pyroxene, biotite, and apatite, with textural differences observed between the two. For example, in the xenoliths from the leucitite host rock, some pyroxene and biotite minerals appear elongated and oriented. In the Q-J diagram, the clinopyroxenes in the xenoliths and host rocks fall within the calcium pyroxene (Quad) range, with compositions spanning from diopside to fassaite. In terms of tectonic context, the xenoliths and host rocks belong to a volcanic arc environment. Most clinopyroxenes in the xenoliths and host rocks crystallized under high oxygen fugacity conditions, at pressures of approximately 5 kbar and water content exceeding 10%. The pyroxenes in xenoliths from the trachytic and leucitite host rocks formed at medium to high pressures, while those in the host rocks formed at low to medium pressures. Micas in the trachytic host rock and its xenoliths are biotite and phlogopite, whereas the micas in the leucitite host rock and its xenoliths predominantly belong to the phlogopite group. The micas in the leucitite host rocks and xenoliths are primary biotites, while those in the trachytic host rocks and xenoliths include both primary and recrystallized biotites. The formation temperatures of clinopyroxenes in the xenoliths and host rocks are estimated to range from 1200$^{\circ C}$ to 1300$^{\circ C}$. The calculated pressures for the xenoliths and host rocks are 6 to 10 kbar, corresponding to depths of approximately 20 to 35 km. For pyroxenite xenoliths in trachytes, the average crystallization pressures are 5.95 and 2.69 kbar, while for those in leucitite, pressures range from 15.65 to 16.18 kbar and 8.66 to 11.36 kbar. In the trachytic host rock, crystallization pressures are 2.6 to 5.10 kbar, while in the leucitite host rock, pressures range from 4.83 to 4.92 kbar and 3.36 to 5.21 kbar. Petrographic evidence suggests that xenoliths in the leucitite host rock originate from greater depths than those in the trachytic host rock. This may be attributed to the deeper initiation of magma crystallization in the leucitite host rock. The similar magnesium numbers of clinopyroxene and biotite in both the xenoliths and host rocks suggest a common initial magma composition. However, subsequent heteromorphism under varying physico-chemical conditions has resulted in different rock types with the same chemical composition. In the spider diagram normalized to the primitive mantle, the host rocks display positive anomalies for incompatible large-ion elements such as Rb, Ba, Th, La, and U, and depletions in Lu, Yb, and Y. This pattern suggests an enriched mantle source, possibly modified by contamination with continental crust materials. Elements such as Ti, Nb, and Ta are sparingly dissolved in metasomatizing fluids originating from oceanic rocks, leading to their accumulation in the dehydrated oceanic crust. Most samples align with the garnet mantle field or are close to it, although the presence of spinel in the mantle is also possible. Regional faults with ENE-WSW left-lateral and SSE-NNW right-lateral motions may have created a transtensional system, facilitating magma generation and ascent. During this ascent, xenoliths from cumulative phases were transported to the Earth's surface by the rising magma.

References

Alavi, M. (1991). Sedimentary and structural characteristics of the Paleo-Tethys remnant in northeastern Iran. *Geological Society of America Bulletin, 103*(7), 983–992. https://doi.org/10.1130/0016-7606(1991)103%3C0983:SASCOT%3E2.3.CO;2

Aldanmaz, E., Pearce, J. A., Thirlwall, M. F., & Mitchell, J. A. (2000). Petrogenetic evolution of late Cenozoic post-collision volcanism in western Anatolia, Turkey. *Journal of Volcanology and Geothermal Research*, *102*, 67–95. https://doi.org/10.1016/S0377-0273(00)00182-7

Aoki, K., & Shiba, I. (1973). Pyroxenes from lherzolite inclusions of Itinome-Gata, Japan. *Lithos, 6*(1), 41–51. https://doi.org/10.1016/0024-4937(73)90078-9

Baker, J. A., Menzies, M. A., Thirlwall, M. F., & MacPherson, C. G. (1997). Petrogenesis of Quaternary intraplate volcanism, Sana'a, Yemen: Implications for plume–lithosphere interaction and polybaric melt hybridization. *Journal of Petrology*, *38*(10), 1359–1390. https://doi.org/10.1093/petroj/38.10.1359

Besharati, P., Kananian, A., & Sepidbar, F. (1999). Pyroxene mineral chemistry in xenoliths of Islamic volcanic rocks (Saray volcano): Evidence from geothermobarometry and the tectonic environment of their formation. *Khwarizmi Earth Sciences*, *8*(2), [Insert page range]. https://doi.org/[Insert DOI if available]

Bina, M. M., Bucur, I., Prevot, M., Meyerfeld, Y., Daly, L., Cantagrel, J. M., & Mergoil, J. (1986). Paleomagnetism, petrology, and geochronology of Tertiary magmatic and sedimentary units from Iran. *Tectonophysics*, *121*, 303–329. https://doi.org/10.1016/0040-1951(86)90050-8

Boudier, F., Ceuleneer, G., & Nicolas, A. (1988). Shear zones, thrusts, and related magmatism in the Oman ophiolite: Initiation of thrusting on an oceanic ridge. *Tectonophysics*, *151*, 275–296. https://doi.org/10.1016/0040-1951(88)90249-1

Boynton, W. V. (1984). Geochemistry of the rare earth elements: Meteorite studies. In P. Henderson (Ed.), *Rare earth element geochemistry* (pp. 63–114). Elsevier. https://cir.nii.ac.jp/crid/1572824499157746944

Deer, W. A., Howie, R. A., & Zussman, J. (1987). *Rock-forming minerals: Single-chain silicates* (2nd ed.). Longman: London. https://books.google.com/books/about/Rock_Forming_Minerals.html?id=x0_kPGjeYcMC

Dehghani, G. A., & Makris, T. (1984). The gravity field and crustal structure of Iran. *Neues Jahrbuch für Geologie und Paläontologie - Abhandlungen*, *168*(2–3), 215–229. https://doi.org/10.1127/njgpa/168/1984/215

Didon, J., & Germain, Y. A. (1976). *Le Sabalan, volcan Plio–Quaternaire de l'Azerbaïdjan oriental (Iran): Étude géologique et pétrographique de l'édifice et de son environnement régional* (Thèse de 3ème cycle). Université scientifique et médicale de Grenoble, France. https://hal.science/tel-00756617/

Emami, M. H. (1990). *Magmatism in Iran*. Geological and Mineral Exploration Organization of the Country. https://library.ngdir.ir/Search/DocumentDetails/372

Fitton, J. G., James, D., & Leeman, W. P. (1991). Basic magmatism associated with Late Cenozoic extension in the western United States: Compositional variations in space and time. *Journal of Geophysical Research, 96*(B8), 13693–13711. https://doi.org/10.1029/91JB00372

Foley, S. (1992). Petrologic characterization of the source components of potassic magmas: Geochemical and experimental constraints. *Lithos, 28*, 187–204. https://doi.org/10.1016/0024-4937(92)90006-K

Frost, D. J. (2006). The stability of hydrous mantle phases. *Reviews in Mineralogy and Geochemistry, 62*(1), 243–271. http://dx.doi.org/10.2138/rmg.2006.62.11

Gertisser, R., & Keller, J. (2000). From basalt to dacite: Origin and evolution of the calc-alkaline series of Salina, Aeolian Arc, Italy. *Contributions to Mineralogy and Petrology, 139*, 607–626. http://dx.doi.org/10.1007/s004100000159

Ghaderi, M., Moayyed, M., Amel, N., & Mojarrad, M. (2020). A new hypothesis on the petrogenesis of Saray volcano with emphasis on formation of sanidine megacryst: Crystallization in an isolated magma chamber. *Scientific Quarterly Journal, Geosciences, 30*(117). http://dx.doi.org/10.22071/GSJ.2019.177151.1630 [In Persian].

Ghadri, M., Amel, N., & Moayed, M. (2022). Mineral chemistry of clinopyroxene, an approach to petrogenesis of Saray Volcanic Complex– Northwest of Iran. *Iranian Geological Quarterly, 16*(61), 45–61. https://sid.ir/paper/963778/en

Ghasemi, A., & Talbot, C. J. (2006). A new tectonic scenario for the Sanandaj-Sirjan Zone (Iran). *Journal of Asian Earth Sciences, 26*, 683–693. https://doi.org/10.1016/j.jseaes.2005.01.003

Green, N. L. (2006). Influence of slab thermal structure on basalt source regions and melting conditions: REE and HFSE constraints from the Garibaldi volcanic belt, northern Cascadia subduction system. *Lithos, 87*, 23–49. https://doi.org/10.1016/j.lithos.2005.05.003

Gurney, J. J., Harte, B., & Cox, K. G. (1975). Mantle xenoliths in the Matsoku kimberlite pipe. *Physics and Chemistry of the Earth, 9*, 507–523. https://doi.org/10.1016/0079-1946(75)90036-1

Hastie, A. R., Kerr, A. C., Pearce, J. A., & Mitchell, S. F. (2007). Classification of altered volcanic island arc rocks using immobile trace elements: Development of the Th–Co discrimination diagram. *Journal of Petrology, 48*(12), 2341–2357. https://doi.org/10.1093/petrology/egm062

Helz, R. T. (1973). Phase relations of basalts in their melting ranges at pH2O=5 kbp_{H_2O} = 5 \, \text{kb}pH2O =5kb as a function of oxygen fugacity: Part I, mafic phases. *Journal of Petrology, 14*(2), 249–302. https://doi.org/10.1093/petrology/14.2.249

Hofmann, A. W. (1997). Mantle geochemistry: The message from oceanic volcanism. *Nature, 385*(6613), 219–229. http://dx.doi.org/10.1038/385219a0

Ilnicki, S. (2010). Petrogenesis of continental mafic dykes from the Izera complex, Karkonosze-Izera Block (West Sudetes, SW Poland). *International Journal of Earth Sciences, 99*, 745–773. https://doi.org/10.1007/s00531-009-0433-5

Jahangiri, A. (2007). Post-collisional Miocene adakitic volcanism in NW Iran: Geochemical and geodynamic implications. *Journal of Asian Earth Sciences, 30*(3–4), 433–447. https://doi.org/10.1016/j.jseaes.2006.11.008

Kargin, A. V., Sazonova, L. V., Nosova, A. A., Lebedeva, N. M., Kostitsyn, Y. A., Kovalchuk, E. V., Tretyachenko, V. V., & Tikhomirova, Y. S. (2019). Phlogopite in mantle xenoliths and kimberlite from the Grib pipe, Arkhangelsk province, Russia: Evidence for multi-stage mantle metasomatism and origin of phlogopite in kimberlite. *Geoscience Frontiers, 10*(6), 1941–1959. https://doi.org/10.1016/j.gsf.2018.12.006

Kopylova, M. G., Russell, J. K., & Cookenboo, H. (1999). Petrology of peridotite and pyroxenite xenoliths from the Jericho kimberlite: Implications for the thermal state of the mantle beneath the Slave craton, northern Canada. *Journal of Petrology, 40*(1), 79–104. https://doi.org/10.1093/petroj/40.1.79

Le Bas, M. J., Le Maître, R. W., Streckeisen, A., & Zanettin, B. (1986). A chemical classification of volcanic rocks based on the total alkali-silica diagram. *Journal of Petrology, 27*(3), 745–750. https://doi.org/10.1093/petrology/27.3.745

Leterrier, J., Maury, R. C., Thonon, P., Girard, D., & Marchal, M. (1982). Clinopyroxene composition as a method of identification of the magmatic affinities of paleo-volcanic series. *Earth and Planetary Science Letters, 59*(1), 139–154. https://doi.org/10.1016/0012-821X(82)90122-4

Lustrino, M., Duggen, S., & Rosenberg, C. L. (2011). The Central–Western Mediterranean: Anomalous igneous activity in an anomalous collisional tectonic setting. *Earth-Science Reviews, 104*(1–3), 1–40. https://doi.org/10.1016/j.earscirev.2010.08.002

McDonough, W. F., & Sun, S. S. (1995). The composition of the Earth. *Chemical Geology, 120*(3–4), 223–253. https://doi.org/10.1016/0009-2541(94)00140-4

McDonough, W. F., & Frey, F. A. (1989). Rare earth elements in upper mantle rocks. In B. R. Lipin & G. A. McKay (Eds.), *Geochemistry and mineralogy of rare earth elements* (Vol. 21, pp. 99–145). Reviews in Mineralogy. https://pubs.geoscienceworld.org/msa/rimg/article/21/1/100/87252/Rare-earth-elements-in-upper-mantle-rocks

McKenzie, D. P., & O'Nions, R. K. (1991). Partial melting distributions from inversion of rare earth element concentrations. *Journal of Petrology, 32*(5), 1021–1091. https://doi.org/10.1093/petrology/32.5.1021

Menzies, M. A., & Wass, S. Y. (1983). CO_2- and LREE-rich mantle below eastern Australia: A REE and isotopic study of alkaline magmas and apatite-rich mantle xenoliths from the Southern Highlands Province, Australia. *Earth and Planetary Science Letters, 65*(3), 287–302. https://doi.org/10.1016/0012-821X(83)90167-X

Merzbacher, C., & Eggler, D. H. (1984). A magmatic geohygrometer: Application to Mount St. Helens and other dacitic magmas. *Geology, 12*(10), 587–590. https://doi.org/10.1130/0091-7613(1984)12

Moayed, M. (2002). A new perspective on the formation of the Neotethys and its relationship with the Tertiary magmatism of the Urmia-Dokhtar and Western Alborz zones - Azerbaijan. *Proceedings of the Sixth National Geological Conference - Shahid Bahonar University of Kerman*, 374–378. https://civilica.com/doc/13616/certificate/print/

Moayed, M., Moazin, M., Kalagari, A. A., & Jahangiri, A. (2004). Petrography and petrology of lamprophyre dykes of the Islamic Peninsula (east of Lake Urmia), East Azerbaijan. *Proceedings of the 8th Conference of the Geological Society of Iran,* Shahrood University of Technology. https://civilica.com/doc/18355/

Moayyed, M., Moazzen, M., Calagari, A. A., Jahangiri, A., & Modjarrad, M. (2008). Geochemistry and petrogenesis of lamprophyric dykes and the associated rocks from Eslamy Peninsula, NW Iran: Implications for deep-mantle metasomatism. *Chemie der Erde*, 68, 141–157. https://doi.org/10.1016/j.chemer.2006.04.002

Moein Vaziri, H. (2002). Petrography and geochemistry of phlogopite-clinopyroxenite enclaves of some young Iranian lavas: Examples from Saray Peninsula, Qorveh, Damavand, and Qale Hasan Ali. *Journal of Sciences of the University of Tehran, 28*(1), 1–17. https://jos.ut.ac.ir/article_16697_4a7d7524151a10c047fb2341036e01a1.pdf

Moine-Vaziri, H. (1985). *Volcanism tertiaire et quaternaire en Iran* (Doctoral dissertation). Université Paris-Sud, Orsay. https://theses.fr/1985PA112187

Moine-Vaziri, H., Khalili Marandi, S. H., & Brousse, R. (1991). Importance d'un volcanism potassique, au Miocene supérieur, en Azerbaijan, Iran. *Comptes Rendus de l'Académie des Sciences, Paris, 313*, 1603–1610. https://pascal-francis.inist.fr/vibad/index.php?action=getRecordDetail&idt=5019082

Moradian ShahrBabak, A. (2007). Geological setting and geochronology of some alkali and calc-alkalic rocks in western (Saray Peninsula) and central (Sourk) Urumieh-Dokhtar Volcanic Belt, Iran. *Earth and Life, 2*(6), 6–20. https://www.researchgate.net/publication/313700459

Morimoto, N., Fabries, J., Ferguson, A., Ginzburg, I. V., Ross, M., Seifert, F. A., Zussman, J., Aoki, K., & Gottardi, G. (1988). Nomenclature of pyroxenes. *Mineralogical Magazine, 52*(367), 535–555. DOI: https://doi.org/10.1180/minmag.1988.052.367.15

Müller, D., Rock, N. M. S., & Groves, D. I. (1992). Geochemical discrimination between shoshonitic and potassic volcanic rocks from different tectonic settings: A pilot study. *Mineralogy and Petrology*, *46*(3-4), 259–289. https://doi.org/10.1007/BF01165769

Nabavi, M. H. (1976). *Introduction to the Geology of Iran.* Geological Organization of the Country Publications. https://www.scirp.org/reference/referencespapers?referenceid=859231

Nachit, H., Ibhi, A., Abia, E. H., & Ohoud, M. B. (2005). Discrimination between primary magmatic biotites, reequilibrated biotites and neoformed biotites. *Comptes Rendus Geoscience, 337*(12), 1415–1420. https://doi.org/10.1016/j.crte.2005.09.014

Nicolas, A. (1989). *Structures in ophiolites and dynamics of oceanic lithosphere.* Kluwer Academic Publishers. https://link.springer.com/book/10.1007/978-94-009-2374-4

Nisbet, E. G., & Pearce, J. A. (1977). Clinopyroxene composition in mafic lavas from different tectonic settings. *Contributions to Mineralogy and Petrology, 63*(2), 149–160. https://link.springer.com/article/10.1007/bf00398776

Novella, D., & Frost, D. J. (2014). The composition of hydrous partial melts of garnet peridotite at 6 GPa: Implications for the origin of Group II kimberlites. *Journal of Petrology*, *55*(11), 2097–2124. https://doi.org/10.1093/petrology/egu059

Patchett, P. J., & Chase, C. G. (2002). Role of transform continental margins in major crustal growth episodes. *Geology, 30*(1), 39–42. https://doi.org/10.1130/0091-7613(2002)030<0039:ROTCMI>2.0.CO;2

Pearce, J. A. (1982). Trace element characteristics of lavas from destructive plate boundaries. In R. S. Thorpe (Ed.), *Andesites* (pp. 230–239). John Wiley & Sons. https://orca.cardiff.ac.uk/id/eprint/8625/

Prelevic, D., Akal, C., Foley, S. F., Romer, R. L., Stracke, A., & Van Den Bogaard, P. (2012). Ultrapotassic mafic rocks as geochemical proxies for post-collisional dynamics of orogenic lithospheric mantle: The case of southwestern Anatolia, Turkey. *Journal of Petrology, 53*(5), 1019–1055. https://doi.org/10.1093/petrology/egs022

Prelevic, D., Foley, S. F., Romer, R., & Conticelli, S. (2008). Mediterranean Tertiary lamproites derived from multiple source components in post-collisional geodynamics. *Geochimica et Cosmochimica Acta, 72*(8), 2125–2156. https://doi.org/10.1016/j.gca.2008.02.003

Prelevic, D., Jacob, D. E., & Foley, S. F. (2013). Recycling plus: A new recipe for the formation of Alpine–Himalayan orogenic mantle lithosphere. *Earth and Planetary Science Letters, 362*, 187–197. https://doi.org/10.1016/j.epsl.2012.11.043

Putirka, K. (2008). Thermometers and barometers for volcanic systems. *Mineralogical Society of America, 69*, 61–120. https://doi.org/10.2138/rmg.2008.69.3

Putirka, K., Ryerson, F. J., & Mikaelian, H. (2003). New igneous thermobarometers for mafic and evolved lava compositions, based on clinopyroxene + liquid equilibria. *American Mineralogist, 88*(10), 1542–1554. DOI:10.2138/am-2003-1017

Rudnick, R. L., & Gao, S. (2003). Composition of the continental crust. In R. L. Rudnick (Ed.), *The crust* (Vol. 3, pp. 1–64). Elsevier-Pergamon. https://www.geol.umd.edu/~rudnick/PDF/Rudnick_Gao_Treatise.pdf

Salters, V. J. M., Longhi, J. E., & Bizimis, M. (2002). Near mantle solidus trace element partitioning at pressures up to 3.4 GPa. *Geochemistry, Geophysics, Geosystems, 3*(7), 1–23. https://doi.org/10.1029/2001GC000262

Saunders, A. D., Norry, M. J., & Tarney, J. (1991). Fluid influence on the trace element composition of subduction zone magmas. *Philosophical Transactions of the Royal Society of London, 335*, 377–392. https://doi.org/10.1098/rsta.1991.0046

Schandl, E. S., & Gorton, M. P. (2002). Application of high field strength elements to discriminate tectonic setting in VMS environment. *Economic Geology, 97*(3), 629–642. https://doi.org/10.2113/97.3.629

Schweitzer, E. L., Papike, J. J., & Bence, A. E. (1979). Statistical analysis of clinopyroxenes from deep-sea basalts. *American Mineralogist, 64*, 501–513. https://doi.org/10.2138/am-1979-5-601

Searle, M. P., & Cox, J. (1999). Tectonic setting, origin, and obduction of the Oman ophiolite. *Geological Society of America Bulletin, 111*(1), 104–122. https://doi.org/10.1130/0016-7606(1999)111%3C0104:TSOOTO%3E2.3.CO;2

Sepidbar, F., Homam, S. M., Shu, Q., Palin, R. M., Besharati, P., & Lustrino, M. (2023). Post-collisional ultrapotassic volcanic rocks and ultramafic xenoliths in the Eslamieh Peninsula, NW Iran: Petrological and geochemical constraints on mantle source and metasomatism. *Lithos, 458-459*, 106261. https://doi.org/10.1016/j.lithos.2023.106261

ShafaiiMoghadam, H., Ghorbani, G., Zaki Khedr, M., Fazlnia, N., Chiaradia, M., Eyuboglu, Y., Santosh, M., Galindo Francisco, C., Lopez Martinez, M., Gourgaud, A., & Arai, S. (2014). Late Miocene K-rich volcanism in the Eslamieh Peninsula (Saray), NW Iran: Implications for geodynamic evolution of the Turkish–Iranian High Plateau. *Gondwana Research, 26*(3), 1028–1050. https://doi.org/10.1016/j.gr.2013.12.002

Shelly, D. (1993). *Igneous and metamorphic rocks under the microscope*. Chapman and Hall. https://rruff.info/doclib/MinMag/Volume_57/57-388-553a.pdf

Soesoo, A. (1997). A multivariate analysis of clinopyroxene composition: Empirical coordinates for the crystallization P-T estimations. *Geological Society of Sweden*, 119(1), 55–60. https://doi.org/10.1080/11035899709546454

Speer, J. A. (1984). Mica in igneous rocks. In S. W. Bailey (Ed.), *Micas* (Vol. 13, pp. 299–356). Reviews in Mineralogy. https://doi.org/10.1515/9781501508820-013

Temel, A., Gondogdu, M. N., & Gourgaud, A. (1998). Petrological and geochemical characteristics of Cenozoic high-K calc-alkaline volcanism in Konya, Central Anatolia, Turkey. *Journal of Volcanology and Geothermal Research, 85*, 327–357. https://doi.org/10.1016/S0377-0273(98)00062-6

Vigouroux, N., Wallace, P. J., & Kent, A. J. (2008). Volatiles in high-K magmas from the western Trans-Mexican Volcanic Belt: Evidence for fluid fluxing and extreme enrichment of the mantle wedge by subduction processes. *Journal of Petrology, 49*(9), 1589–1618. https://doi.org/10.1093/petrology/egn039

Whitney, D. L., & Evans, B. W. (2010). Abbreviations for names of rock-forming minerals. *American Mineralogist, 95*(1), 185–187. DOI:10.2138/am.2010.3371

Wood, D. A. (1980). The application of a Th-Hf-Ta diagram to problems of tectonomagmatic classification and to establishing the nature of crustal contamination of basaltic lavas of the British Tertiary Volcanic Province. *Earth and Planetary Science Letters, 56*, 11–30. https://doi.org/10.1016/0012-821X(80)90116-8

Yang, J. H., Chung, S. L., Wilde, S. A., Wu, F., Chu, M. F., Lo, C. H., & Fan, H. (2005). Petrogenesis of post-orogenic syenites in the Sulu orogenic belt, East China: Geochronological, geochemical and Nd–Sr isotopic evidence. *Chemical Geology*, *214*, 99–125. https://doi.org/10.1016/j.chemgeo.2004.08.053

Zeng, G., Chen, L.-H., Xu, X.-Sh., Jiang, Sh.-Y., & Hofmann, A. W. (2010). Carbonated mantle sources for Cenozoic intra-plate alkaline basalts in Shandong, North China. *Chemical Geology*, *273*, 35–45. https://doi.org/10.1016/j.chemgeo.2010.02.009